2015

Retrieval of aerosol microphysical properties from AERONET photopolarimetric measurements: 2. A new research algorithm and case demonstration

Xiaoguang Xu
University of Nebraska–Lincoln, xxu@umbc.edu

Jun Wang
University of Nebraska–Lincoln, jwangjun@gmail.com

Jing Zeng
University of Nebraska–Lincoln

Robert Spurr
RT Solutions Inc., Cambridge, Massachusetts

Xiong Liu
Harvard-Smithsonian Center for Astrophysics, Cambridge, Massachusetts

See next page for additional authors

AGU PUBLICATIONS

JGR

Journal of Geophysical Research: Atmospheres

RESEARCH ARTICLE
10.1002/2015JD023113

This article is a companion to *Xu and Wang* [2015] doi:10.1002/2015JD23108.

Key Points:
- A new aerosol retrieval algorithm for AERONET polarimetric measurements
- Retrieve size and refractive index for both fine- and coarse-mode aerosols
- Promising results with real data, limitations, and next research steps discussed

Correspondence to:
J. Wang,
jwangjun@gmail.com

Citation:
Xu, X., et al. (2015), Retrieval of aerosol microphysical properties from AERONET photopolarimetric measurements: 2. A new research algorithm and case demonstration, *J. Geophys. Res. Atmos.*, *120*, 7079–7098, doi:10.1002/2015JD023113.

Received 14 JAN 2015
Accepted 8 MAY 2015
Accepted article online 8 JUN 2015
Published online 29 JUL 2015

Retrieval of aerosol microphysical properties from AERONET photopolarimetric measurements: 2. A new research algorithm and case demonstration

Xiaoguang Xu[1], Jun Wang[1], Jing Zeng[1], Robert Spurr[2], Xiong Liu[3], Oleg Dubovik[4], Li Li[5], Zhengqiang Li[5], Michael I. Mishchenko[6], Aliaksandr Siniuk[7], and Brent N. Holben[7]

[1]Earth and Atmospheric Sciences, University of Nebraska–Lincoln, Lincoln, Nebraska, USA, [2]RT Solutions Inc., Cambridge, Massachusetts, USA, [3]Harvard-Smithsonian Center for Astrophysics, Cambridge, Massachusetts, USA, [4]Laboratoire d'Optique Atmosphérique, CNRS–Université de Lille 1, Villeneuve d'Ascq, France, [5]State Environmental Protection Key Laboratory of Satellites Remote Sensing, Institute of Remote Sensing and Digital Earth of Chinese Academy of Sciences, Beijing, China, [6]NASA Goddard Institute for Space Studies, New York, New York, USA, [7]NASA Goddard Space Flight Center, Greenbelt, Maryland, USA

Abstract A new research algorithm is presented here as the second part of a two-part study to retrieve aerosol microphysical properties from the multispectral and multiangular photopolarimetric measurements taken by Aerosol Robotic Network's (AERONET's) new-generation Sun photometer. The algorithm uses an advanced UNified and Linearized Vector Radiative Transfer Model and incorporates a statistical optimization approach. While the new algorithm has heritage from AERONET operational inversion algorithm in constraining a priori and retrieval smoothness, it has two new features. First, the new algorithm retrieves the effective radius, effective variance, and total volume of aerosols associated with a continuous bimodal particle size distribution (PSD) function, while the AERONET operational algorithm retrieves aerosol volume over 22 size bins. Second, our algorithm retrieves complex refractive indices for both fine and coarse modes, while the AERONET operational algorithm assumes a size-independent aerosol refractive index. Mode-resolved refractive indices can improve the estimate of the single-scattering albedo (SSA) for each aerosol mode and thus facilitate the validation of satellite products and chemistry transport models. We applied the algorithm to a suite of real cases over Beijing_RADI site and found that our retrievals are overall consistent with AERONET operational inversions but can offer mode-resolved refractive index and SSA with acceptable accuracy for the aerosol composed by spherical particles. Along with the retrieval using both radiance and polarization, we also performed radiance-only retrieval to demonstrate the improvements by adding polarization in the inversion. Contrast analysis indicates that with polarization, retrieval error can be reduced by over 50% in PSD parameters, 10–30% in the refractive index, and 10–40% in SSA, which is consistent with theoretical analysis presented in the companion paper of this two-part study.

1. Introduction

The present study, as the second paper in a two-part study, aims at developing an inversion algorithm that retrieves microphysical properties of atmospheric aerosols using multispectral and multiangular photopolarimetric observations, such as those collected as part of the new research development for the Aerosol Robotic Network (AERONET). With over 400 locations around the word, most AERONET sites are equipped with an automatic Sun and sky scanning spectral radiometer, or the CIMEL-318 type Sun photometer, to measure direct and diffuse solar radiation in various atmospheric window channels [*Holben et al.*, 1998]. The direct Sun radiance data are used to infer the spectral aerosol optical depth (AOD), with an uncertainty of ~0.01 [*Holben et al.*, 1998; *Smirnov et al.*, 2000]. By performing observations at dozens of viewing geometries in the solar aureole and the principal plane, AERONET also measures the diffuse solar radiation for a wide range of scattering angles. These sky radiance data are used in the current AERONET operational inversion algorithm [*Dubovik and* King, 2000; *Dubovik et al.*, 2006, hereafter Dubovik00&06] to derive (1) the aerosol particle size distribution (PSD) in terms of the aerosol volume (in the atmospheric column) at 22 size bins, (2) the fractional volume of nonspherical particles, and (3) the complex refractive index ($m_r - m_i i$) assumed to be independent of particle size. From those microphysical parameters, the Dubovik00&06 algorithm computes the aerosol single-scattering albedo (SSA or ω_A) and the phase

function. Uncertainties in the AERONET inversion products are 15–100% for the bin-based PSD parameters, 0.025–0.05 for m_r and ~ 0.03 for ω_A [*Dubovik et al*., 2000].

While the AERONET AOD and other inversion products have been widely used to study the climatology of aerosol optical properties [*Dubovik et al*., 2002; *Levy et al*., 2007a] and for the development and validation of aerosol retrieval algorithms for satellite sensors such as the Moderate Resolution Imaging Spectrometer (MODIS) [*Kaufman et* al., 1997; *Remer et al*., 2005; *Levy et al*., 2007b, 2010; *Wang et al*., 2010] and the Multi-angle Imaging Spectroradiometer [*Diner et al*., 1998; *Kahn et al*., 2010], the AERONET operational algorithm also faces (a) challenges in evaluation of aerosol data either retrieved from newer-generation satellite sensors or simulated from chemistry transport models and (b) opportunities to improve the retrieval through the use of multispectral polarization measurements that are now available at a few sites and will be made available at more sites as part of the AERONET future research development (http://aeronet.gsfc.nasa.gov). These challenges and opportunities, as further described below, are also the motivation for us to develop a new research algorithm.

The first challenge is that newer-generation satellite sensors are expected to offer aerosol microphysical products with accuracy that is equivalent to, if not higher than, that of the current AERONET microphysical products. For instance, the Aerosol Polarimetry Sensor (APS) for the NASA Glory mission, through measuring the first three Stokes vector elements simultaneously from 250 viewing angles at nine spectral bands (410, 443, 556, 670, 865, 910, 1370, 1610, and 2200 nm), was designed to retrieve aerosol effective radius (r_{eff}), effective variance (v_{eff}), and spectral complex index of refraction for both fine and coarse modes [*Mishchenko et al*., 2007]. While no actual product is available because of the failure of Glory launch, several case studies with the APS's prototype airborne sensor, RSP (the Remote Sensing Polarimeter), demonstrated feasibility of APS algorithm [*Chowdhary et al*., 2002, 2005; *Mishchenko et al*., 2004; *Waquet et al*., 2009]. At least in the case of spherical particles, the accuracy of APS's bimodal aerosol products was expected to be 10% for r_{eff}, 40% for v_{eff}, 0.02 for m_r, and 0.03 for the SSA (ω_A) [*Mishchenko et al*., 2007]. Some of these accuracy expectations are unlikely to be matched by existing ground-based and in situ instruments, including those at the AERONET sites. Moreover, the current AERONET retrieval of the refractive index and the ω_A are not recommended to use when the 440 nm AOD is lower than 0.4 [*Holben et al*., 2006] due to expected limited accuracy identified in the detailed sensitivity study by *Dubovik et al*. [2000].

The second challenge is associated with the inconsistency in assumptions of PSD that exists between current AERONET inversion products and satellite retrievals on the one hand, as well as the aerosol models used by climate models on the other hand. Specifically, the Dubovik00&06 algorithm retrieves the aerosol PSD on in 22 discrete size bins. In contrast, a continuous PSD function (e.g., lognormal) is usually assumed in satellite retrieval algorithms, such as those for APS/RSP [*Mishchenko et al*., 2007; *Waquet et al*., 2009] and the POLDER/PARASOL algorithm [*Hasekamp et al*., 2011]. Also, aerosol microphysical properties are usually calculated with continuous PSD assumptions in many chemistry transport models, such as GEOS-Chem [*Drury et al*., 2010; *Wang et al*., 2010] and the Goddard Chemistry Aerosol Radiation and Transport model [*Chin et al*., 2002]. Clearly, the actual aerosol PSD is never a perfect lognormal distribution, but neither is it discrete. At least from the scattering perspective, the aerosol PSD can be well characterized with an effective radius r_{eff} and an effective variance v_{eff}, while the specific function of the PSD is shown to be much less important [*Hansen and Travis*, 1974]. In other words, since the retrieval is based on the information content in the particle optical scattering, the most relevant size parameters, regardless of the PSD shape, should be r_{eff} and v_{eff}, at least for spherical particles.

The third challenge is that the assumption of a size-independent refractive index (and SSA) in Dubovik00&06 is not in line with the majority of counterpart satellite retrieval algorithms [e.g., *Mishchenko et al*., 2007; *Hasekamp et al*., 2011; *Martonchik et al*., 2009], which often uses different refractive indices for various individual aerosol modes. In many cases, tropospheric aerosol is a mixture of modes with substantially different refractive indices. For example, smoke from biomass burning can be mixed with mineral dust over western coastal North Africa [*Yang et al*., 2013]. Furthermore, the assumption of size-independent refractive index can lead to errors in the retrieval of the size distributions when the refractive indices for fine- and coarse-mode aerosols differ substantially [*Dubovik et al*., 2000; *Chowdhary et al*., 2001]. Thus, a mode-resolved parameterization of the refractive index in an aerosol retrieval algorithm not only can

facilitate the validation of satellite products and chemistry transport models but also is expected to improve the accuracy of PSD and SSA retrievals for each mode. *Dubovik et al*. [2000] have tested the possibility of retrieving separated refractive indices of fine and coarse modes; however, they concluded that the retrieval of bimodal refractive indices is essentially nonunique due to limited information in the AERONET radiance-only observations.

The retrieval algorithm proposed here embraces the future opportunities of deploying polarization measurements through AERONET and ameliorates the aforementioned limitations in the Dubovik00&06 algorithm by incorporating both radiance and polarization data. Polarization measurements contain valuable information on aerosol microphysical properties [*Mishchenko and Travis*, 1997], as the polarization of the scattered light is highly sensitive to aerosol size and refractive index [*Hansen and Travis*, 1974; *Mishchenko et al*., 2002]. As suggested by the information content analysis in the companion paper [*Xu and Wang*, 2015], adding polarization data into the AERONET inversion will enable the retrieval of bimodal refractive index and SSA even for 440 nm AOD as low as 0.2 when the Ångström exponents (AE) is between 0.7 and 1.6. We also found that the uncertainty in the retrieval can be reduced by up to 76% (49%), 69% (52%), 66% (46%), and 49% (20%) for the fine mode (coarse mode) r_{eff}, v_{eff}, m_{r}, and SSA, respectively. We note, however, the conclusions of above mentioned studies [*Hansen and Travis*, 1974; *Mishchenko and Travis*, 1997; *Xu and Wang*, 2015] were based on consideration of spherical aerosol particles and were primarily from a theoretical point of view. In contrast, the studies by *Dubovik et al*. [2006] and *Deuzé et al*. [1993, 2001] revealed serious limitation of polarimetric retrieval of the properties for the coarse mode, especially nonspherical aerosols. Moreover, *Dubovik et al*. [2006] have shown that while the polarimetic observation of fine particles and large spheres are highly sensitive to the real part of refractive index, even they have nonnegligible sensitivity to particle shape. Therefore, adding polarization measurements to the inversion has great potential to improve the accuracy of AERONET microphysical retrievals, provided that the difficulty of representing aerosol particle shapes is recognized or adequately addressed. In these regards, most of the past efforts seem to suggest clear improvements in characterization of fine-mode aerosol using polarimetric observations. For example, *Li et al*. [2009], based upon the Dubovik00&06 algorithm, demonstrated the possibility to reduce errors in the fine-mode size distribution, real part of the refractive index, and particle shape parameters.

Section 2 of this paper gives an overview of the algorithm, while sections 3 and 4, respectively, describe in detail the forward modeling of AERONET photopolarimetric measurements and the inversion strategies. Retrieval results for a collection of real cases are presented and discussed in section 5, followed by a brief conclusion in section 6. It should be noted that our focus is on the development of core components for a new research algorithm that can be used for the next-generation AERONET, although also considered are the practical aspects of implementing this algorithm, including quality assurance, dynamical surface polarimetric reflectance, and dynamic gas absorption. Our future work will address other aspects needed to transition this research algorithm into operational form, including the code efficiency and performance.

2. General Structure of the Algorithm

Figure 1 gives an overview of the retrieval algorithm specifically designed for the analysis and inversion of photopolarimetric remote sensing observations, such as those from AERONET. The algorithm builds upon the UNified and Linearized Vector Radiative Transfer Model (UNL-VRTM), which consists of seven component modules for the forward simulation of observations and a module for optimal inversion [*Wang et al*., 2014]. The forward modeling includes the linearized vector radiative transfer model (VLIDORT) developed by *Spurr* [2006], a linearized Mie code and a linearized T-Matrix code calculating aerosol single-scattering properties [*Spurr et al*., 2012], a module calculating Rayleigh scattering and a module for gas absorption, plus a surface model computing bidirectional reflectance/polarization distribution function (BRDF/BPDF) [*Spurr,* 2004]. The required input parameters for the algorithm are the relevant atmospheric profiles (of pressure, temperature, and gaseous mixing ratio), aerosol loading in terms of AOD or aerosol columnar volume, aerosol vertical profiles, aerosol microphysical and chemical parameters (size distribution and complex refractive index), and surface reflection parameters. The users can specify up to two modes of the aerosol population. Each mode is characterized by the total particle number (or volume), the vertical profile, size distribution, and refractive index. The aerosol-related modules—Mie, T-matrix, and

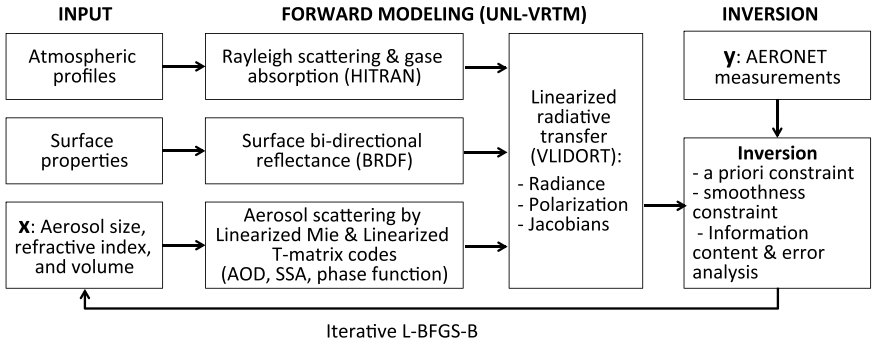

Figure 1. Overview of our inversion algorithm.

VLIDORT—are analytically linearized and fully coupled. Thus, the forward model not only simulates radiance and/or polarization for a given spectrum but also computes the Jacobians of these radiation fields with respect to input aerosol microphysical parameters. Our inversion-oriented framework supplies these Jacobians together with observation error characterizations and a priori constraints to the statistical optimization procedure for the retrieval. Information content and error analysis are also included in the procedure along with the inversion. Although our algorithm is tailored to measurements from the AERONET Sun photometer, its modularized framework enables the simulation and inversion of observations from various platforms, including satellite sensors.

Development of the inversion component in our algorithm was built upon our experience with optimization of aerosol emissions using the adjoint chemistry transport model (CTM) [*Wang et al.*, 2012; *Xu et al.*, 2013]. In essence, the optimization method is consistent with the adjoint modeling that constrains aerosol emissions from measurements through inverting a CTM, although different physical processes are involved for inversion of AERONET observation. Both inversions seek the optimal solutions for a state vector that minimizes the differences between the model simulation and observation. In addition, our algorithm inherits the inversion strategy from the Dubovik00&06 algorithm, in particular with regard to the smoothness constraint on the spectral dependence of the complex refractive index.

3. Forward Modeling of AERONET Observations

The aerosol retrieval algorithm is designed to invert photopolarimetric measurements of the direct and diffuse solar radiation measurements obtained with the ground-based CIMEL Dual-Polar Sun/sky radiometer, or the CE318-DP Sun photometer, operated at the Beijing_RADI site since 2009; it also served as part of the UAE^2 (abbreviation for the Unified Aerosol Experiment-United Arab Emirates) field campaigns [*Reid et al.*, 2008; *Eck et al.*, 2008]. This new-generation instrument performs programmed scanning sequences similar to those of the older-generation CE318 radiometer but now has the capability to measure polarization over an extended spectrum with central wavelengths ranging from 340 to 1640 nm [*Li et al.*, 2013, 2014]. Table 1 summarizes the currently available measurements. Briefly, the instrument performs direct Sun observations in various spectral bands between 340 and 1640 nm at standard 15 min or 0.25 air mass intervals, from which the AOD is derived. Basic sky measurements of diffuse radiances are made in 340, 380, 440, 500, 675, 870, 1020, and 1640 nm bands via two observational sequences: in the solar almucantar (ALM) and in the solar principal plane (PPL). More than eight ALM sequences are made daily at optical air masses of 4, 3, 2, and 1.7 both in the morning and in the afternoon; each sequence is performed at constant solar elevation for up to 72 specified azimuth angles relative to the position of the Sun. The PPL sequence includes the measurements of diffuse radiances for a

Table 1. AERONET Observation Characteristics

Symbol	Parameter	Instrumental Uncertainty	Other Uncertainties
y_1	Direct Sun AOD	0.01–0.02	~0.02 spatial/temporal variation
y_2	Sky radiance in solar almucantar	5%	Surface BRDF and BPDF
y_3	Sky radiance in principal plane	5%	Surface BRDF and BPDF
y_4	DOLP in principal plane	0.01	Surface BRDF and BPDF

set of 42 scattering angles, and observations are made hourly when the optical air mass is less than 2. Polarization measurements (PPP) are taken at the same wavelengths, and the scan sequence is made in the principal plane at 5° increments between viewing zenith angles of −85° and 85°. A full observation set thus consists of about 20 min of scans: 30 s direct Sun, followed by 5 min for ALM sky radiances, then the 5 min PPL sky radiances, and finally, the 8 min PPP sky polarization measurements. Given the AERONET instrumental characteristics, we require an accurate and comprehensive vector radiative transfer model that treats the gaseous absorption, aerosol scattering, and surface reflection in order to simulate a complete set of such observations.

The radiance and polarization of light at any wavelength can be represented by a Stokes column vector **I** having four elements [*Hansen and Travis*, 1974]

$$\mathbf{I} = [I, Q, U, V]^T, \tag{1}$$

where I is the total intensity (radiance), Q and U describe the state of linear polarization, V describes the state of circular polarization, and T indicates a transposed matrix. It should be noted that all radiation fields and optical parameters used in this paper are functions of the light wavelength λ. For simplicity, however, we omit λ in all formulas. The degree of linear polarization (DOLP) is defined by

$$\mathrm{DOLP} = \frac{\sqrt{Q^2 + U^2}}{I}. \tag{2}$$

In the solar principal plane, U is negligibly small for a homogeneous atmosphere and the above formula becomes DOLP = − Q/I. Its deviation from zero is an indicator of a lack of homogeneity or instrumental issues [*Li et al.*, 2014]. Let $\mathbf{I}_0 = [I_0, 0, 0, 0]^T$ denote the Stokes vector for incident solar radiation at the top of the atmosphere (TOA) from the direction (θ_0, ϕ_0), where θ_0 and ϕ_0 are the solar zenith and azimuth angles, respectively. For a plane-parallel atmosphere bounded below by a reflective surface, the vector radiative transfer equation in the medium for the specific intensity column vector **I** of light propagating in the viewing direction (θ, ϕ) can be written [*Hovenier et al.*, 2004; *Mishchenko et al.*, 2002]

$$\mu \frac{\partial \mathbf{I}(\tau, \mu, \phi)}{\partial \tau} = \mathbf{I}(\tau, \mu, \phi) - \mathbf{J}(\tau, \mu, \phi; \mu_0, \phi_0); \tag{3}$$

$$\begin{aligned} \mathbf{J}(\tau, \mu, \phi; \mu_0, \phi_0) = {} & \frac{\omega}{4\pi} \int_{-1}^{1} \int_{0}^{2\pi} \mathbf{P}(\tau, \mu, \mu_0, \phi - \phi_0) \mathbf{I}(\tau, \mu_0, \phi_0) \mathrm{d}\phi_0 \mathrm{d}\mu_0 \\ & + \frac{\omega}{4\pi} \mathbf{P}(\tau, \mu, \mu_0, \phi - \phi_0) \mathbf{I}_0 \exp(-\tau/\mu_0). \end{aligned} \tag{4}$$

Here τ is the extinction optical depth measured from TOA, μ and μ_0 are cosines of θ and θ_0, respectively, ω is the SSA, and **P** is the phase matrix. The first term in equation (4) represents multiple scattering contributions, while the second indicates scattered light from the direct solar beam.

Parameters required to solve the above radiative transfer equation are τ, ω, and $\mathbf{P}(\boldsymbol{\Theta})$ for the atmosphere, and the reflectance matrix $\mathbf{R}_s(\mu, \phi; \mu_0, \phi_0)$ of the underlying surface. Considering a cloud-free atmosphere, the solar radiation is attenuated by molecular scattering, gaseous absorption, and aerosol scattering and absorption. For a given layer, we have

$$\tau = \tau_\mathrm{A} + \tau_\mathrm{R} + \tau_\mathrm{G} \tag{5}$$

$$\omega = \frac{\tau_\mathrm{A}\omega_\mathrm{A} + \tau_\mathrm{R}}{\tau} \tag{6}$$

$$\mathbf{P}(\boldsymbol{\Theta}) = \mathbf{P}_\mathrm{A}(\boldsymbol{\Theta}) \frac{\tau_\mathrm{A}\omega_\mathrm{A}}{\tau_\mathrm{A}\omega_\mathrm{A} + \tau_\mathrm{R}} + \mathbf{P}_\mathrm{R}(\boldsymbol{\Theta}) \frac{\tau_\mathrm{R}}{\tau_\mathrm{A}\omega_\mathrm{A} + \tau_\mathrm{R}} \tag{7}$$

where τ_A, τ_R, and τ_G are optical depth, respectively, by aerosol extinction, Rayleigh scattering of air density fluctuations, and gaseous absorption. ω_A is the SSA of aerosol, and $\mathbf{P}_\mathrm{A}(\boldsymbol{\Theta})$ and $\mathbf{P}_\mathrm{R}(\boldsymbol{\Theta})$ are, respectively, the aerosol and Rayleigh phase matrices as functions of the scattering angle $\boldsymbol{\Theta}$. The forward modeling of radiance/polarization measurements thus requires knowledge of single-scattering properties for aerosols and air density fluctuations, absorption of trace gases, and reflectance/polarization by surface. Modules to deal with these requirements are described in detail by *Wang et al.* [2014]. Here we briefly summarize those components that are particularly important for our algorithm in this study.

3.1. Surface Representation

Although surface reflectance has in general a low influence on downwelling sky radiances and polarization, a state-of-the-art representation of the surface reflectivity potentially reduces model uncertainties, especially for measurements taken at low-elevation angles that could be affected by surface diffusion. The reflectance calculation in the UNL-VRTM uses a linearized BRDF package from *Spurr* [2004], in which the BRDF is a linear combination of up to three semiempirical kernel functions. Specifically, we utilize the spectral BRDF parameters from the MODIS surface products that are operationally reported every 16 days at a 1 km resolution [*Lucht et al*., 2000]. The MODIS BRDF product supplies three weighting parameters (f_{iso}, f_{vol}, and f_{geo}) for the first seven MODIS bands, respectively, corresponding to three kernel types: isotropic, Ross-Thick (K_{vol}), and Li-Sparse (K_{geo}):

$$\rho_R(\mu, \phi; \mu_0, \phi_0) = f_{iso} + f_{vol}K_{vol}(\mu, \phi; \mu_0, \phi_0) + f_{geo}K_{geo}(\mu, \phi; \mu_0, \phi_0) \tag{8}$$

Expanded expressions for K_{vol} and K_{geo} appear in *Wanner et al*. [1995] and *Lucht et al*. [2000]. Here we use time-matched MODIS BRDF products at wavelengths of 464 nm, 650 nm, 865 nm, and 1240 nm to reconstruct the bidirectional reflectance over AERONET stations at wavelengths of 440 nm, 675 nm, 870 nm, and 1020 nm.

Studies have shown that the BPDF for land surfaces is generally rather small and is "spectrally neutral" [*Nadal and Breon,* 1999; *Maignan et al*., 2004, 2009; *Waquet et al*., 2007; *Litvinov et al*., 2011]. Most empirical BPDF models are based on Fresnel coefficients of light reflectance from the surface. Here we have incorporated the one-parameter model developed by *Maignan et al*. [2009], which was derived from analyses of several years of POLDER/PARASOL measurements. This model describes the polarized reflectance at any viewing geometry (μ, ϕ) from the given incident geometry (μ_0, ϕ_0) as

$$\boldsymbol{\rho}_P(\mu, \phi; \mu_0, \phi_0) = \frac{C_0 \exp(-\tan\alpha)\exp(-\mathrm{NDVI})}{\mu_0 + \mu}\mathbf{F}_p(\alpha, n_v) \tag{9}$$

where C_0 is a constant parameter chosen for a certain surface type, α is half of the phase angle of reflectance, n_v is the refractive index of vegetation (the value 1.5 is used here), and $\mathbf{F}_p$ is the Fresnel reflection matrix. We chose a spectrally independent value for C_0 based on the recommendations by *Maignan et al*. [2009] for relevant surface types.

The combination of the BRDF and BPDF for land surface follows the discussion by *Dubovik et* al. [2011]. The surface reflectance matrix $\mathbf{R}_s(\mu, \phi; \mu_0, \phi_0)$ is represented as a sum of diffuse unpolarized reflectance and specular reflectance; the former is modeled using the MODIS BRDF in equation (8), and the latter using the BPDF formula in equation (9). It should be noted that, however, these BRDF and BPDF specifications in our algorithm have limited accuracy. To mitigate this effect, our inversion algorithm has an option to quantify the impacts of uncertainties in assumed BRDF/BPDF parameters on simulated radiances, and to include these model parameter errors the inversion, this is discussed in more detail in the companion paper [*Xu and Wang*, 2015].

3.2. Molecular Scattering and Absorption

The Rayleigh scattering optical depth in any atmospheric layer (τ_R) is based on the Rayleigh cross-section computation following *Bodhaine et al.* [1999]. The Rayleigh phase matrix depends upon molecular anisotropy through the depolarization factor, also computed from the same source. We use the line-by-line approach [*Liou*, 2002] by accumulating each individual absorption line to simulate molecular absorption spectra. While the UNL-VRTM can account for as many as 22 trace gases, we consider only the most influential trace species for the AERONET spectral bands: H_2O (vapor), O_3, NO_2, O_2 (O_2-O_2 collision), and CO_2. Calculation of their absorption optical depth (τ_G) utilizes the line-spectroscopic absorption parameters (for H_2O and CO_2) and a UV cross-section library (for O_3, NO_2, and O_2-O_2) archived in the HITRAN database [*Orphal and* Chance, 2003; *Rothman et al*., 2009]. In our algorithm, the columnar amounts of O_3 and NO_2 are dynamically adjusted with retrievals from the Ozone Monitoring Instrument (OMI) [*Levelt et al*., 2006] on board the AURA satellite. We apply the columnar water vapor amount retrieved from the 940 nm radiances measured by the same Sun photometer [*Halthore et al*., 1997].

3.3. Aerosol Single-Scattering Properties

Aerosol single-scattering properties can be calculated either with a Mie code [*de Rooij and van der Stap*, 1984] or a T-matrix code [*Mishchenko et al.*, 1996, *Mishchenko and Travis,* 1998]; both codes have been linearized [*Spurr et al.*, 2012] and integrated in the UNL-VRTM [*Wang et al.*, 2014]. However, we use the linearized Mie code alone for both fine- and coarse-aerosol modes, since the linearized T-matrix program has computational difficulty for nonspherical aerosols of the coarse-mode size levels considered in this study and given the shape of nonspherical particles is unknown. This assumption applies to stations dominated by spherical aerosols like smoke, sulfate, and sea salt, whereas it may mischaracterize the aerosol microphysical properties if substantial amount of nonspherical particles (like mineral dust) present. However, it is hard to tell quantitatively how much of an error could be incurred by our spherical assumption given the shapes of nonspherical particles are not unique and difficult to characterize. *Wang et al.* [2003] showed that even in dust-dominated cases, spherical particles also contribute significantly to the scattering of radiation in the atmosphere.

The required inputs for the Mie code are the PSD function parameters and complex refractive index ($m_r - m_i i$). In agreement with many studies [e.g., *Schuster et al.*, 2006; *Waquet et al.*, 2009], we assume that the aerosol volume distribution follows a bimodal lognormal function

$$\frac{dV}{d\ln r} = \sum_{i=1}^{2} \frac{V_0^i}{\sqrt{2\pi}\ln\sigma_g^i} \exp\left[-\frac{\left(\ln r - \ln r_v^i\right)^2}{2\ln^2\sigma_g^i}\right] \tag{10}$$

where V_0, r_v, and σ_g are the total volume concentration, volume median radius, and geometric standard deviation, respectively. The superscript i indicates the size mode and later will be replaced by "f" for fine mode and "c" for coarse mode. We assume that particle size ranges from 0.01 to 10 nm for the fine mode and from 0.05 to 20 nm for the coarse mode, both covering $> 99.9\%$ of the total volume of an idealistic size range $(0, +\infty)$. An advantage of the lognormal distribution is that standard deviations for the number, area, and volume PSD functions are identical, and therefore allowing that the median radii for these PSD functions can be converted from one to another [*Seinfeld and Pandis*, 2006]. For instance, the volume median radius r_v relates to the number geometric median radius r_g by $r_v = r_g \exp(3\ln^2\sigma_g)$. The r_{eff} and v_{eff} are related to the geometric parameters through:

$$\begin{cases} r_{eff} = r_v \ \exp\left(-\frac{1}{2}\ln^2\sigma_g\right) \\ v_{eff} = \exp\left(\ln^2\sigma_g\right) - 1 \end{cases} \tag{11}$$

The linearized Mie code computes the aerosol extinction efficiency factor Q_{ext}, single-scattering albedo ω_A, and phase matrix $\mathbf{P}_{aer}(\mathbf{\Theta})$, as well as Jacobians of these quantities with respect to input parameters including r_{eff}, v_{eff}, m_r, and m_i. The phase matrix and its Jacobians are expressed in terms of the coefficients $\mathbf{B}_l(\mathbf{\Theta})$ for each moment l in terms of the generalized spherical function expansions for each nonzero phase matrix element. Let $\mathbf{\Lambda}$ denotes the vector of aerosol microphysical parameters, $\mathbf{\Lambda} = [V_0, r_{eff}, v_{eff}, m_r, m_i]^T$, and $\mathbf{M}$ the vector of aerosol optical parameters, $\mathbf{M} = [\tau_A, \omega_A, \mathbf{B}_l(\mathbf{\Theta})]^T$, where τ_A is related to Q_{ext} by $\tau_A = \frac{3V_0 Q_{ext}}{4r_{eff}}$. The Mie code acts as an operator that maps vector $\mathbf{\Lambda}$ to $\mathbf{M}$. The Jacobian matrix of $\mathbf{M}$ with respect to $\mathbf{\Lambda}$, or $\frac{\partial \mathbf{M}}{\partial \mathbf{\Lambda}}$, is calculated by means of the Mie code's linearization feature.

3.4. Radiative Transfer

The radiative transfer equation (3) is solved with the Vector Linearized Discrete Ordinate Radiative Transfer (VLIDORT) model, which is a core part of the UNL-VRTM. VLIDORT, developed by *Spurr* [2006], is a linearized pseudospherical vector discrete ordinate radiative transfer model for multiple scattering of diffuse radiation in a stratified multilayer atmosphere. It computes four elements of the Stokes vector $\mathbf{I}$ for downwelling and upwelling radiation at any desired atmospheric level. The VLIDORT includes the pseudospherical approximation to calculate solar beam attenuation in a curved medium. It also uses the delta-M approximation for dealing with sharply peaked forward scattering. The calculated Stokes vector has been fully verified against other radiative transfer models for various scattering atmospheres [*Wang et al.*, 2014]. Specifically for the AERONET inversion, we consider 16 discrete ordinate streams in the radiative transfer calculation and retain 180 terms in the spherical function expansion of the scattering matrix to ensure accurate calculation of diffuse radiation.

Table 2. State Vector Elements and Associated Constraints for Inversion[a]

Symbol	Parameter	A Priori Constraint?	Smoothness Constraint?
V_0^f, V_0^c	Columnar volume ($\mu m^3\ \mu m^{-2}$)	√	
r_{eff}^f, r_{eff}^c	Effective radius (μm)	√	
v_{eff}^f, v_{eff}^c	Effective variance	√	
m_r^f, m_r^c	Real part refractive index	√	√
m_i^f, m_i^c	Imaginary refractive index	√	√

[a]The superscripts, c and f, respectively, denote fine- and coarse-aerosol modes. Refractive indices are for spectral wavelengths of 440, 675, 870, and 1020 nm.

Along with the Stokes vector **I**, VLIDORT also computes the Jacobian matrix of **I** with respect to aerosol optical vector **M**, $\frac{\partial \mathbf{I}}{\partial \mathbf{M}}$. Therefore, the combination of the VLIDORT and the Linearized Mie codes allows for a direct calculation of the Jacobian matrix of the Stokes vector with respect to aerosol microphysics $\mathbf{\Lambda}$ by

$$\frac{\partial \mathbf{I}}{\partial \mathbf{\Lambda}} = \frac{\partial \mathbf{I}}{\partial \mathbf{M}} \frac{\partial \mathbf{M}}{\partial \mathbf{\Lambda}} \tag{12}$$

Essentially, the above equation can yield the derivatives of the radiance I and DOLP with respect to any aerosol microphysical parameter, i.e., $\frac{\partial I}{\partial \mathbf{\Lambda}}$ and $\frac{\partial \mathrm{DOLP}}{\partial \mathbf{\Lambda}}$. While obtaining $\frac{\partial I}{\partial \mathbf{\Lambda}}$ is straightforward, $\frac{\partial \mathrm{DOLP}}{\partial \mathbf{\Lambda}}$ can be derived from equation (2) as follows:

$$\frac{\partial \mathrm{DOLP}}{\partial \mathbf{\Lambda}} = -\frac{\mathrm{DOLP}\frac{\partial I}{\partial \mathbf{\Lambda}}}{I} + \frac{Q\frac{\partial Q}{\partial \mathbf{\Lambda}} + U\frac{\partial U}{\partial \mathbf{\Lambda}}}{I\sqrt{Q^2+U^2}} \tag{13}$$

In addition, VLIDORT also calculates the Jacobians of I and DOLP with respect to surface property parameters characterizing the BRDF/BPDF kernels from equations (8) and (9). All of these Jacobians from the UNL-VRTM are required for the inversion algorithm, and all of them have been fully validated against partial derivatives calculated by finite differences [*Wang et al.*, 2014].

4. Inversion Strategies

4.1. Basic Formulation of the Inverse Problem

Let **x** denote a *state vector* of n parameters to be retrieved and **y** an *observation vector* assembled by m measurements, and let **F** indicate a *forward model* that describes the physics of the measurement process. Then, we can express the relationship between the observation vector and the state vector as

$$\mathbf{y} = \mathbf{F}(\mathbf{x}) + \boldsymbol{\epsilon}, \tag{14}$$

where $\boldsymbol{\epsilon}$ is an experimental error term that includes observation noise and forward modeling uncertainty.

For this study, the observation vector **y** comprises components from different sources. As listed in Table 1, there are up to four categories of observations, i.e., the direct -Sun AOD, the sky radiance around the solar aureole, the sky radiance in the solar principal plane, and the DOLP in the solar principal plane, with all measurements performed at 440, 675, 870, and 1020 nm. Also indicated in Table 1 are the calibration errors and other measurement uncertainties that make of the term $\boldsymbol{\epsilon}$. The state vector **x** comprises aerosol microphysical parameters associated with the bimodal lognormal PSD function, including r_{eff}, v_{eff}, V_0, and $m_r - m_i i$ at 440, 675, 870, and 1020 nm (Table 2). All parameters include both the fine and coarse modes and account for a total of 22 elements ($n = 22$). The forward modeling of AERONET observations is a complex process with a large number of internal parameters. The inversion of the state vector from these measurements is an ill-posed problem due to the nonlinearity and limited sensitivity of the observed radiative quantities to retrieval parameters. We need to add constraints to make the problem amenable to inversion.

4.2. Combining A Priori and Smoothness Constraints

A priori information describes our knowledge of the state vector before measurements are applied, and an a priori constraint is commonly used to achieve a well-defined stable and physically reasonable solution to an ill-posed problem. Usually, a priori knowledge comprises both a mean state $\mathbf{x}_a$ and its error $\boldsymbol{\epsilon}_a$:

$$\mathbf{x} = \mathbf{x}_a + \boldsymbol{\epsilon}_a. \tag{15}$$

One of the satisfactory sources for the a priori knowledge is a climatology based on historical measurements. For a given AERONET site, we use the available inversion products that have been obtained with the Dubovik00&06 algorithm, for which the a priori can be well characterized by the mean values and standard deviations of each component in the state vector. At the same time, the a priori can also be determined from other sources if a historical AERONET retrieval is not available. For example, we could extract aerosol microphysical climatology from chemistry transport model simulations [e.g., *Wang et al.*, 2010] or from measurements of in situ and/or even satellite sensors.

Among those retrieved parameters, the aerosol volumes—V_0^f and V_0^c—are the most variable or uncertain quantities. A reasonable initial guess for these quantities could speed up the iterative inversion. As presented in the following, we obtain their initial guesses from the AOD measurements at two spectral wavelengths. Given the a priori information on the aerosol PSD and refractive indices, the aerosol extinction efficiency Q_{ext} can be obtained for each fine mode and coarse mode with the Mie code. Then the AOD (τ_A) is related to the aerosol volumes via

$$\tau_A = \tau_A^f + \tau_A^c = \frac{3V_0^f Q_{ext}^f}{4r_{eff}^f} + \frac{3V_0^c Q_{ext}^c}{4r_{eff}^c}. \tag{16}$$

Clearly, applying the above equation to the AODs at any two spectral wavelengths, we can easily solve V_0^f and V_0^c. Considering the component fraction is more sensitive to the wavelength dependency of AOD at longer wavelengths (Figure 2b), we choose AODs at 870 nm 1020 nm to determine the initial guesses of V_0^f and V_0^c.

For some parameters, the a priori estimates may be poorly known, but these parameters behave smoothly with no sharp oscillations. For example, the aerosol refractive index usually does not vary rapidly over the visible to near-infrared spectral range. In this regard, a smoothness constraint could be a preferable addition. The technique of constraining a smooth solution was pioneered by *Philips* [1962] and *Twomey* [1963] and has been successfully used to retrieve coherent aerosol size distributions [*Dubovik and King,* 2000] and atmospheric vertical profiles [*Twomey*, 1977]. The principle of the smoothness constraint is to restrain the degree of nonlinearity of a certain physical parameter by limiting the values of its dth derivatives:

$$\mathbf{G}_d\mathbf{x} + \boldsymbol{\epsilon}_\Delta = 0, \tag{17}$$

where $\mathbf{G}_d$ is a differential matrix composed of coefficients for calculating the dth derivatives of $\mathbf{x}$ with respect to the dependent variable and the vector $\boldsymbol{\epsilon}_\Delta$ indicates uncertainties in these derivatives.

In particular, for constraining the dependence of the spectral refractive index with wavelength, the matrix $\mathbf{G}_d$ calculates the dth difference of the refractive index at four wavelengths (440, 675, 870, and 1020 nm). As discussed by *Dubovik and King* [2000], we assume a linear relationship between the logarithm of the refractive index and the logarithm of the wavelength: $m_r \sim \lambda^{-\alpha}$ and $m_i \sim \lambda^{-\beta}$. Further, the matrix $\mathbf{G}_1$ for the *first* difference (of either m_r or m_i of one mode) can be expressed as

$$\begin{aligned}\mathbf{G}_1 &= \begin{bmatrix} 1/\Delta\lambda_1 & 0 & 0 \\ 0 & 1/\Delta\lambda_2 & \\ 0 & 0 & 1/\Delta\lambda_3 \end{bmatrix} \begin{bmatrix} -1 & 1 & 0 & 0 \\ 0 & -1 & 1 & 0 \\ 0 & 0 & -1 & 0 \end{bmatrix} \\ &= \begin{bmatrix} -1/\Delta\lambda_1 & 1/\Delta\lambda_1 & 0 & 0 \\ 0 & -1/\Delta\lambda_2 & 1/\Delta\lambda_2 & 0 \\ 0 & 0 & -1/\Delta\lambda_3 & 1/\Delta\lambda_3 \end{bmatrix}\end{aligned} \tag{18}$$

Here $\Delta\lambda_1$, $\Delta\lambda_2$, and $\Delta\lambda_3$ are the denominators for the first-order differences in the logarithm, e.g., $\Delta\lambda_1 = \ln\frac{675}{440}$. As to $\boldsymbol{\epsilon}_\Delta$, we assume errors in first differences of the refractive index following *Dubovik and King* [2000], i.e., 0.2 for m_r and 1.5 for m_i.

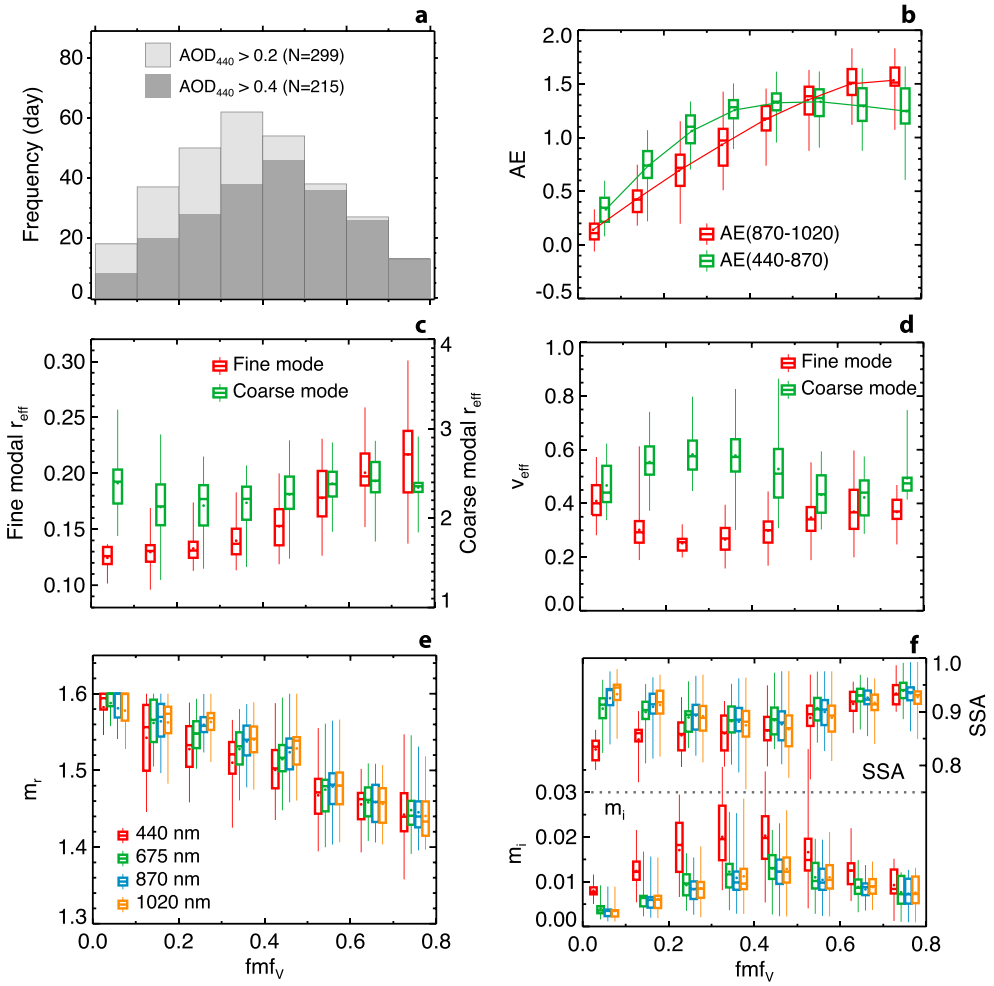

Figure 2. Climatology of aerosol properties over the Beijing_RADI site derived from AERONET daily inversion products during 2011–2013. The variables are shown as functions of the fine-mode fraction in terms of the aerosol volume, or fmf_V. Eight bins are applied for fmf_V from 0 to 0.8 with an increment of 0.1. Quantities in each box-whisker include the median (dash in the box), the mean (dot), the 25th to 75th percentiles (box), and the minimum to maximum (whiskers) for each fmf_V bin. The six panels are (a) histogram of used data; (b) the Ångström exponents (AE) derived from 870 to 1020 nm (red) and from 440 to 870 nm (green) wavelength pairs; (c) the effective radius for aerosols in the fine (red) and coarse (green) mode; (d) the effective variance in the fine (red) and coarse (green) mode (green); (e) the real part of the refractive index at 440, 675, 870, and 1020 nm; and (f) the imaginary part of the refractive index and aerosol SSA at the same wavelengths.

Similar to the approach suggested by *Dubovik and King* [2000], we use multiple a priori constrains in the retrieval. Specifically, we combine the a priori constraint of equation (15) and the smoothness constraint of equation (17); our inverse problem is equivalent to solving the following equation set:

$$\begin{cases} \mathbf{y}_j = \mathbf{F}_j(\mathbf{x}) + \boldsymbol{\epsilon}_j, & \text{for } j = 1,\ 2,\ \ldots J \\ \mathbf{x} = \mathbf{x}_a + \boldsymbol{\epsilon}_a \\ 0 = \mathbf{G}_d\mathbf{x} + \boldsymbol{\epsilon}_\Delta \end{cases}, \tag{19}$$

where j indicates any observation category as listed in Table 1.

4.3. Statistical Optimized Inversion

Under the assumption of Gaussian-distributed errors, the optimized solution of equation (19) according to the Maximum Likelihood method corresponds to the state vector that minimizes the quadratic cost function consisting of multiple terms [*Dubovik and King*, 2000; *Dubovik*, 2004],

$$\Psi(\mathbf{x}) = \frac{1}{2}\sum_{j=1}^{J}\gamma_j\left[\mathbf{F}_j(\mathbf{x}) - \mathbf{y}_j\right]^T\mathbf{S}_{\epsilon_j}^{-1}\left[\mathbf{F}_j(\mathbf{x}) - \mathbf{y}_j\right] + \frac{1}{2}\gamma_a(\mathbf{x} - \mathbf{x}_a)^T\mathbf{S}_a^{-1}(\mathbf{x} - \mathbf{x}_a) + \frac{1}{2}\gamma_\Delta\,\mathbf{x}^T\boldsymbol{\Omega}\,\mathbf{x}, \tag{20}$$

where T indicates the transpose operation, $\mathbf{S}_{\epsilon j}$ is the error covariance matrix of the measurements $\mathbf{y}_j$, $\mathbf{S}_a$ is the error covariance matrix of the a priori estimate, $\mathbf{\Omega}$ is a smoothing matrix related to $\mathbf{G}_d$ and the error covariance matrix $\mathbf{S}_\Delta$ (of the dth derivatives of $\mathbf{x}$) by $\mathbf{\Omega} = \mathbf{G}_d^T \mathbf{S}_\Delta^{-1} \mathbf{G}_d$. γ_j, γ_a, and γ_Δ are regularization parameters. Here we assume that error is independent between measurements and that a priori error is also independent between retrieved parameters, which results in zero off-diagonal elements for matrices $\mathbf{S}_{\epsilon j}$ and $\mathbf{S}_a$. In principle, the minimization of three-term cost function given by the equation (20) is conceptually analogous to the minimization of bicomponent cost functions generally considered in the Bayesian approach [*Rodgers*, 2000]. These three terms on the right-hand side of equation (20) represent, respectively, (1) the total squared fitting error incurred owing to departures of the model predictions from the observations, (2) the penalty error incurred owing to departures of the estimates from the a priori, and (3) the penalty error incurred owing to departures from the defined smoothness feature. Overall, the minimization of $\Psi(\mathbf{x})$ achieves the objective of improving the agreement between the model and the measurements while ensuring that the solution remains within a reasonable range and degree of smoothness.

The regularization parameters in the calculation of $\Psi(\mathbf{x})$ act as weights to balance the fitting error and the penalty errors. Clearly, a good assignment of these regularization parameters is of crucial importance for the statistical optimal solution. High values of γ_a and γ_Δ can lead to oversmoothing of the solution with little improvement to the fitting residuals, while low values minimize the error term at the cost of greatly increasing the parameter penalty terms. In this study, we assume equal weights for observational constraint term and combined a priori constrain terms in the cost function following *Dubovik* [2004]:

$$\gamma_a = \frac{1}{2} n^{-1}, \quad \gamma_\Delta = \frac{1}{2}(n_\Delta - d)^{-1}, \quad \text{and} \quad \gamma_j = J^{-1} m_j^{-1} \text{ for } j = 1, \ldots, J. \tag{21}$$

Here n is the number of retrieved parameters, d is the order of difference, and n_Δ is the number of state elements that are supplied with smoothness constraints. Values for γ_j are chosen to control the fitting residuals for used observations from four different groups as listed in Table 1. Each group comprises the number of m_j observations for j from 1 to the number of used groups (J). The value of γ_j for the jth group is $\gamma_j = J^{-1} m_j^{-1}$, which means the observation quadratic term is normalized by the observation count of each category.

In principle, solving this inverse problem is tantamount to a pure mathematical minimization procedure. Considering the nonlinearity of the forward modeling, we perform the minimization of $\Psi(\mathbf{x})$ with an iterative quasi-Newton approach using the L-BFGS-B algorithm [*Byrd et al.*, 1995; *Zhu et al.*, 1994; *Xiao and Zhang*, 2008], which offers bounded minimization to ensure the solution stays within a physically reasonable range. The L-BFGS-B algorithm requires knowledge of $\mathbf{x}$ and $\Psi(\mathbf{x})$, as well as the gradient of $\Psi(\mathbf{x})$ with respect to $\mathbf{x}$, $\frac{\partial \Psi}{\partial \mathbf{x}}$. By linearizing the forward model $\mathbf{F}(\mathbf{x})$, we can determine $\frac{\partial \Psi}{\partial \mathbf{x}}$ by

$$\frac{\partial \Psi}{\partial \mathbf{x}} = \sum_{j=1}^{J} \gamma_j \mathbf{K}_j^T \mathbf{S}_{\epsilon_j}^{-1} \left[\mathbf{F}_j(\mathbf{x}) - \mathbf{y}_j \right] + \gamma_a \mathbf{S}_a^{-1} (\mathbf{x} - \mathbf{x}_a) + \gamma_\Delta \mathbf{\Omega}\, \mathbf{x}, \tag{22}$$

where $\mathbf{K}_j$ is the Jacobian matrix of $\mathbf{F}_j(\mathbf{x})$ with respect to $\mathbf{x}$, which is computed analytically by equations (12) and (13). At each iteration, improved estimates of the state vector are implemented and the forward simulation is recalculated. The convergence criterion to determine the optimal solution is the smallness of the $\Psi(\mathbf{x})$ reduction and the norm of $\frac{\partial \Psi}{\partial \mathbf{x}}$. The iteration stops when the reduction of $\Psi(\mathbf{x})$ is less than 1% within 10 continuous iterations. Then, the optimal solutions are identified corresponding to the smallest norm of $\frac{\partial \Psi}{\partial \mathbf{x}}$ from these 10 last iterations. In addition, to ensure a physically reasonable solution, we also perform retrieval error analysis and impose a practical quality control on real measurements.

4.4. Retrieval Error Analysis

The retrieval without error characterization is of significantly lesser value. Once the retrieval is achieved, the retrieval error can be characterized by the a posteriori state, and the error analysis can be performed in terms of a linearization of the problem around the solution $\hat{\mathbf{x}}$. We estimate the retrieval error on each state vector element using the error covariance matrix of the a posteriori state:

$$\hat{\mathbf{S}}^{-1} = \sum_{j=1}^{J} \hat{\mathbf{K}}_j^T \mathbf{S}_{\epsilon_j}^{-1} \hat{\mathbf{K}}_j + \mathbf{S}_a^{-1} + \mathbf{\Omega}, \tag{23}$$

where $\hat{\mathbf{K}}_j$ is the Jacobian matrix of the forward model $\mathbf{F}_j(\mathbf{x})$ at the solution $\hat{\mathbf{x}}$. It should be noted that the above three-term a posteriori formularized according to the cost function defined in equation (20) but without applying regularization parameters. Therefore, regularization only applies in the inversion for the search of optimal solution. We estimate a posteriori error in the nonregularized space once the solution is achieved. Simply, the retrieval error for each element can be estimated by

$$\hat{\epsilon}_i = \hat{\mathbf{S}}_{i,i}^{\frac{1}{2}}. \tag{24}$$

With $\hat{\mathbf{S}}$, we can also estimate the uncertainty in parameters (such as ω_A and asymmetry factor in this study) that can be fully determined by the parameters in $\mathbf{x}$ but are not themselves directly retrieved. If such a parameter is a function defined by $\xi = \xi(\mathbf{x})$, then the uncertainty of ξ is [*Rodgers*, 2000]

$$\hat{\epsilon}_\xi = \sqrt{\sum_{i=1}^{n}\sum_{j=1}^{n}\hat{\mathbf{S}}_{i,j}\frac{\partial\xi}{\partial x_i}\frac{\partial\xi}{\partial x_j}} \tag{25}$$

4.5. Quality Control of Measurements

We apply a suite of quality criteria to ensure (a) a cloud-free condition, (b) that aerosol particles are quasi-homogeneously distributed in the horizontal plane within the scanning region, and (c) the measurements are densely populated and cover a wide range of scattering angles so that they provide sufficient information to retrieve all parameters falling within specified uncertainty levels. More specifically, these criteria are as follows: (i) the number of AOD observations ≥ 2 within a ±25 min centered at the period of a full scan sequence; (ii) sky radiance observations are excluded when the scattering angle is less than 3.2° and DOLP observations are excluded when the scattering angle is smaller than 5°; (iii) a symmetry check for the ALM radiances: the difference is less than 5% for the azimuthal angle of 180° and less than 10% elsewhere; and (iv) PPL and PPP observations are discarded when their second derivatives with respect to the scattering angle are beyond the smoothing threshold. Although most of these criteria follow *Holben et al.* [2006], we also check the smoothness of the principal plane radiances and DOLP to identify scans that are contaminated by cloud. We apply the threshold on the second derivative of radiance (or DOLP) with respect to scattering angle in order to restrain local oscillations of radiance (or DOLP) caused by clouds or heterogeneous aerosol plumes. Thus, applying such a threshold can effectively remove sharp kinks and ensure continuous quantities in the PPL and PPP sequences. Indeed, this smoothness check shares the same principle to the smoothness constraint presented in the section 4.2.

5. Demonstration With Real AERONET Observations

5.1. Selected Cases and the A Priori Characterization

We applied our algorithm to the radiance and polarization measured by the CIMEL CE318-DP Sun photometer (instrument #350) at Beijing_RADI (116.37°E, 40.00°N), which is a joint station of the AERONET and the Sun/sky-radiometer Observation NETwork. The AOD measurements are designated from the field-calibrated level 1.5 products. Measurements of the direct and diffuse radiance as well as DOLP were performed at eight spectral wavelengths, with the measurements at 440, 675, 870, and 1020 nm chosen for the inversion. The sky radiances were calibrated following *Li et al.* [2008] and are reported as values normalized by the extraterrestrial solar irradiance. The DOLP were calibrated in the laboratory following *Li et al.* [2010]. Measurement uncertainties were estimated to be 0.01–0.02 for AOD, 3–5% for radiance, and 0.01 for DOLP.

The a priori is characterized with the *climatology* of aerosol properties derived from the version 2.0 AERONET daily inversion products of the same site during 2011–2013. These daily products are averages of up to eight individual inversions within a day. The PSD parameters were analyzed with 299 available daily inversions when the 440 nm AOD is larger than 0.2. The refractive index and SSA were analyzed with 215 inversions when the 440 nm AOD is larger than 0.4. In Figure 2, the variables are shown as functions of the fine-mode fraction in terms of the aerosol volume, or fmf_V. It can be found that the fmf_V from 0.2 to 0.6 accounts for ~70% of occurrences (Figure 2a), indicating aerosol over this site is dominated by the mixed fine-coarse aerosols. The AE derived from the 1020 nm and 870 nm AOD pairs is more linearly related to the fmf_V than the 440 nm and 870 nm AE (Figure 2b), because AE over the longer-wavelength pairs is more sensitive to the component fraction and less sensitive to the change of component particle size [*Schuster et al.*, 2006].

Table 3. Main Characteristics of Case Studies in this Work

Case	Date and Time UTC	θ_0 (°)	τ_{440}	AE (870–1020 nm)	OMI NO_2 (molecules/cm^2)	OMI O_3 (DU)	Vapor (cm)
A	02/22/2011 04:30	50.3–50.6	3.46	1.57	6.3×10^{16}	356.5	0.86
B	03/17/2013 03:25	43.0–42.2	2.74	1.39	4.2×10^{16}	332.7	0.76
C	03/22/2013 07:23	57.0–60.0	1.05	1.01	4.1×10^{16}	386.7	1.01

From Figures 2c and 2d, we determine the a priori ($\mathbf{x}_a$) of PSD parameters for both fine and coarse modes based on their mean values across all fmf_V intervals. For refractive index, we pick their mean values when $fmf_V < 0.2$ for the coarse mode and when $fmf_V > 0.6$ for the fine mode (Figures 2e and 2f). Along with determining $\mathbf{x}_a$, we estimate the a priori error (ϵ_a) for each parameter (very right column of Table 6) as two standard deviations for a 95% confidence interval. Then we build $\mathbf{S}_a$ with zero off-diagonal elements by neglecting the error correlation between retrieved parameters. In addition, we found in the Figure 2e that the m_r retrievals decrease quasi-linearly with the increasing fmf_V, which indicates the m_r has distinct values between aerosols in the fine and the coarse modes over this site. It is expected that the m_r in the mixed aerosol situations, e.g., $0.3 < fmf_V < 0.6$, is also expected to have the distinct values for fine- and coarse-mode particles.

With the above a priori characterization, we performed retrievals for three cases, respectively, on 22 February 2011, 17 March 2013, and 22 March 2013 (hereinafter, cases A–C). A brief characterization of these cases is presented in Table 3. Indeed, these cases represent different aerosol mixtures: (A) dominated by fine particles, (B) well mixed, and (C) dominated by large particles. Moreover, the present algorithm is designed to run with two inversion scenarios: the first includes DOLP, while the second ignores it—hereafter, we label these scenarios type P and I, respectively. An examination of the difference in the fitting results between these two types of inversion would indicate the value of DOLP in improving the retrieval. For all cases, optimal solutions are achieved within less than thirty iterations, and further iterations yield negligible reduction of the cost function. Below we discuss the fitting residuals in section 5.2 and the retrieved results in section 5.3. A contrast analysis is presented in section 5.4 to demonstrate the superiority of the inversion involving polarization.

5.2. Fitting Residuals

The fitting residual characterizes the disagreement between the model and the measurement. The individual sky radiance residual is defined as a relative quantity:

$$e_I = (I_{calc} - I_{meas})/I_{meas}, \tag{26}$$

where I_{calc} and I_{meas} denote the calculated (using the retrieved aerosol parameters) and measured sky radiances, respectively. In contrast, the fitting residuals for AOD and DOLP are defined by

$$e_{AOD} = AOD_{calc} - AOD_{meas}, \tag{27}$$

$$e_{DOLP} = DOLP_{calc} - DOLP_{meas}. \tag{28}$$

The residual errors for AOD, sky radiance, and DOLP are mean values of $|e_I|$, $|e_{AOD}|$, and $|e_{DOLP}|$, respectively.

Because similar fitting results are found for these three aerosol types (cases), we illustrate in Figure 3 the fitting results for sky radiances and DOLP only for the case B. We found that retrievals from both types of inversion can well reproduce these AERONET measurements of AOD and sky radiances. Fitting residuals from both types of inversions for individual ALM radiance measurement lie within the experimental uncertainty of 5%, although the fit of radiances from the P-type inversion is slightly deteriorated: residual error is 1.60% for the P type compared to 1.46% for the I-type inversion. However, the DOLP residual error can be much larger for the I-type inversion than that for the P-type inversion: 0.011 versus 0.004. The statistical residual errors for all three cases are displayed in Table 4. As these fitting results show, without the constraints imposed by polarization, the retrieved aerosol microphysical parameters could result in larger error in polarization simulations, highlighting the necessity to include polarization in the inversion as an additional source of constraint.

5.3. Retrieved Aerosol Properties

Figure 4 displays our retrievals from both I-type and P-type inversions for the aerosol volume PSD and complex refractive indices. Also shown are the retrievals from the AERONET Dubovik00&06 inversion. Table 5 presents the values of the (P-type inversion) retrieved PSD parameters including V_0, r_{eff}, v_{eff}, r_V, and

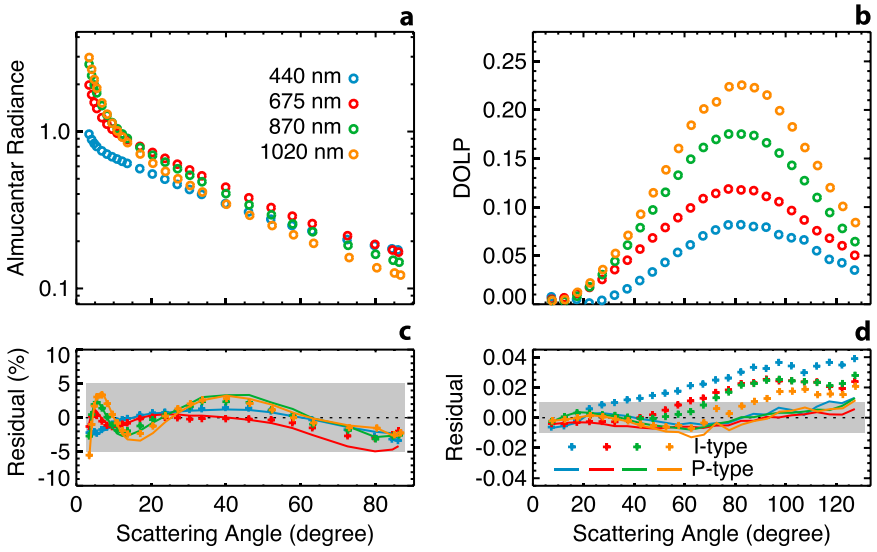

Figure 3. (a) Measured almucantar normalized radiances. (b) Measured DOLP in the solar principal plane. (c) Fitting residuals for almucantar radiances by the P-type inversion (solid curves) and I-type inversion (crosses). (d) Same as Figure 3c but for the fitting residuals of principal plane DOLP. Four colors indicate different wavelengths: blue for 440 nm, green for 675 nm, red for 870 nm, and orange for 1020 nm. Gray areas in Figures 3c and 3d indicate the measurement uncertainty.

σ_g for both fine and coarse modes and corresponding values from the Dubovik00&06 inversion. The PSD in these cases consists of separated fine- and coarse-aerosol modes. In the cases dominated by fine-mode aerosol (A) and well-mixed aerosol (B), our retrievals agree with the AERONET inversions, though marginal differences are found in the effective radius and standard deviation. In case C dominated by coarse-mode aerosols, our algorithm results in a smaller-coarse mode r_{eff} than that from the AERONET algorithm; this may be caused by our assumption of spherical particles, whereas the Dubovik00&06 algorithm considers nonsphericity for coarse particles. We did not find significant differences in the aerosol volumes between our algorithm and the Dubovik00&06 algorithm. As Figures 4b–4c indicate, fine-mode volume retrieved by the P-type inversion is lower than that retrieved by the I-type inversion; such an overestimation from radiance-only inversion was also found by *Li et al.* [2009].

In contrast with the Dubovik00&06 algorithm, which retrieves a single refractive index for each spectrum that is independent of aerosol size, our retrieved aerosol refractive indices pertain to the corresponding fine and coarse modes. In order to get a general impression of the agreement between our retrievals and the AERONET inversions, we compute the bulk refractive index that is a weighted average by the particle volume of each mode in our retrieval [e.g., *Wang and Martin*, 2007]. According to Figures 4d–4f, while the bulk value of m_r is in good agreement (differences < 0.03) with that of the Dubovik00&06 retrievals, our retrieval allows for a mode-resolved characterization of aerosol refractive index. For instance, the aerosol m_r has values 1.5–1.6 in the coarse mode, which is larger than that in the fine mode (1.4–1.5). A *T*-Test using the corresponding retrieving standard errors indicates a statistical significance level of about 98% for the difference of real part refractive indices between the fine and coarse modes. In addition, we found that the P-type inversion usually yields higher values of m_r compared to the I-type inversion; this finding agrees with *Li et al.* [2009] in that the radiance-only inversion underestimates m_r.

Table 4. Summary of Measurement Fitting Errors

Case	Inversion Type	AOD Residual Error	Radiance Residual Error	DOLP Residual Error
A	I	0.0008	1.78%	0.008
	P	0.0015	1.85%	0.005
B	I	0.0007	1.46%	0.011
	P	0.0005	1.60%	0.004
C	I	0.0006	2.67%	0.020
	P	0.0021	3.11%	0.009

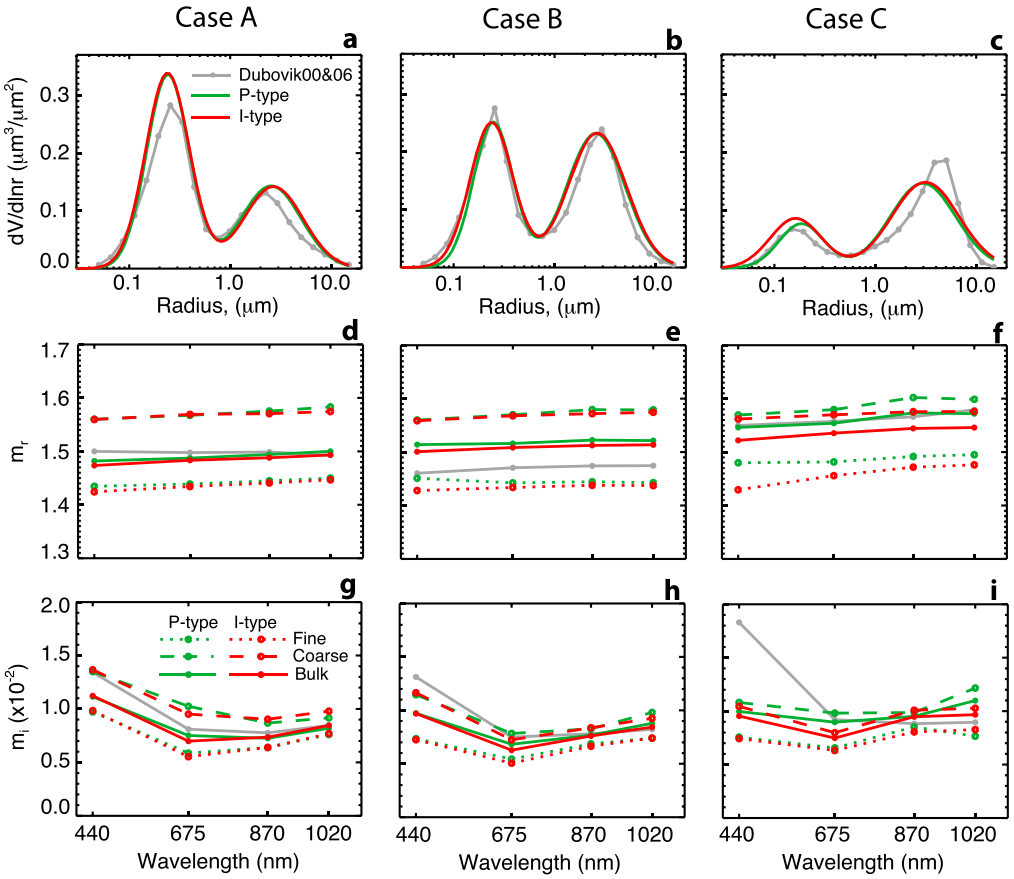

Figure 4. Retrieved aerosol volume size distribution (PSD) and refractive index compared with Dubovik00&06 inversions (gray). P-type and I-type inversions are represented by green and red colors, respectively. In Figures 4d–4i, the retrievals are shown for aerosols in both fine (dotted) and coarse (dashed) modes, as well as bulk averages (solid). The PSD relevant quantities for Figures 4a–4c are summarized in Table 5.

According to Figures 4g–4i, the bulk m_i retrieved by our algorithm is consistent overall with that from the Dubovik00&06 algorithm, with both retrievals showing similar spectral dependencies. One exception is for case C; m_i at 440 nm is about 0.01 from our algorithm but is about 0.02 with the Dubovik00&06 algorithm. As expected, our inversion algorithm also offers mode-resolved m_i. We notice in our retrieval that m_i shows an increasing dependence on the spectral wavelength for the fine mode but a decreasing tendency for the coarse mode.

Table 5. PSD-Related Parameters Retrieved by our P-Type Inversion, Compared With Values From the AERONET Dubovik00&06 Inversion

		Case A		Case B		Case C	
	Units	Ours	AERONET	Ours	AERONET	Ours	AERONET
V_0^f	$\mu m^3\ \mu m^{-2}$	0.41	0.36	0.28	0.31	0.10	0.09
r_{eff}^f	μm	0.215	0.208	0.223	0.201	0.163	0.156
v_{eff}^f	-	0.26	0.32	0.23	0.32	0.30	0.33
r_v^f	μm	0.242	0.240	0.246	0.232	0.186	0.179
σ_g^f	-	1.62	1.69	1.57	1.69	1.67	1.70
V_0^c	$\mu m^3\ \mu m^{-2}$	0.24	0.21	0.39	0.32	0.28	0.26
r_{eff}^c	μm	2.02	2.01	2.05	2.26	2.24	2.61
v_{eff}^c	-	0.59	0.53	0.55	0.38	0.75	0.50
r_v^c	μm	2.55	2.44	2.57	2.65	2.97	3.28
σ_g^c	-	1.98	1.92	1.94	1.76	2.12	1.89

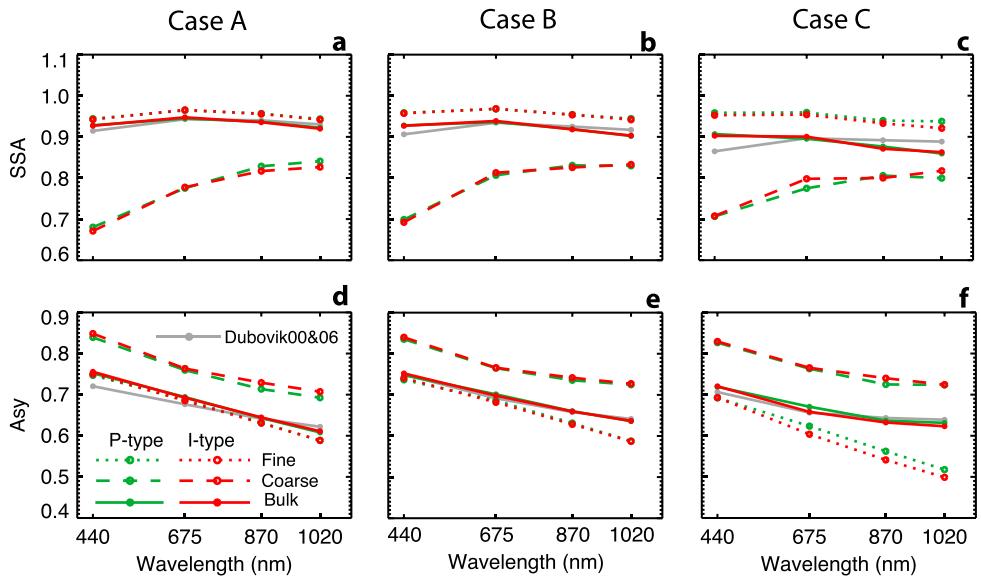

Figure 5. Same as Figure 4 but for derived aerosol SSA and Asy.

In the forward modeling framework, the aerosol macrophysical optical properties act as intermediate model parameters to link the aerosol microphysical characteristics to the radiation fields. These macrophysical optical parameters include but are not limited to the aerosol SSA (ω_A), the scattering phase function, and the asymmetry factor (Asy). These quantities do not appear in the state vector; instead, they can be derived from the retrieved microphysical parameters, and are thus called derived or intermediate parameters. In Figure 5, we present ω_A and Asy from our retrieval and the comparison with their counterparts from the Dubovik00&06 inversion. In our retrieval, bulk values of ω_A and Asy are again calculated by a scatter-weight averaging of the fine- and coarse-mode values. We found that the bulk ω_A and Asy from our algorithm and the Dubovik00&06 algorithm agree very well. However, our retrieved coarse-mode ω_A varies from 0.7 to 0.9, increasing with wavelength. In contrast, the retrieved fine-mode ω_A runs close to 0.9.

5.4. Improvement Over Radiance-Only Retrievals

The above comparisons of retrieval results confirm that both P- and I-type inversions by our algorithm can generate solutions quite consistent with the current Dubovik00&06 algorithm. In order to demonstrate the improvements in the retrieval by including polarization, we compare the retrieval errors between the P-type and I-type inversions in Table 6 for individual aerosol parameters. Also compared are the errors in the derived ω_A and Asy. Clearly, the P-type inversion yields lower retrieval errors for all the retrieved and derived parameters; this is confirmed by the theoretical analysis in the companion paper of this two-part series [*Xu and Wang*, 2015]. The key points from the comparison are

1. Polarization measurements provide important constraints in improving the retrieval of V_0, r_{eff}, and v_{eff} for both fine- and coarse-aerosol modes. For these three cases, the errors in the retrieved V_0 with polarization are less than 3% for the fine mode and less than 5% for the coarse mode, representing a significant decrease from their counterparts (~15% and ~10%) in the I-type inversion. Adding polarization can also decrease the error in r_{eff} of both fine and coarse modes from 8–14% for the I-type inversion to 3% and below. Errors in v_{eff} retrieved by the P-type inversion are 8–12% for aerosol in the fine mode and 11–26% in the coarse mode, whereas they can exceed 50% with the I-type inversion.
2. Polarization measurements also provide useful constraints in improving the refractive index retrievals. The most significant improvement is found in the fine-mode m_r, where the error is lower than 0.01 for the P-type inversion, compared to 0.02–0.03 for the I-type inversion. The error in the coarse-mode m_r from P-type inversion ranges from 0.04 to 0.06, depending on the prevalence of coarse-mode particles. For retrieving m_i, the inclusion of polarization reduces the error by 10–30%, a value also depending on coarse-mode dominance.

Table 6. Errors on the Retrieved and Derived Parameters From Both Types of Inversion[a]

	Case A		Case B		Case C		
	$\hat{\epsilon}_P$	$\hat{\epsilon}_I$	$\hat{\epsilon}_P$	$\hat{\epsilon}_I$	$\hat{\epsilon}_P$	$\hat{\epsilon}_I$	ϵ_a
V_0^f	1.9%	12%	2.1%	13%	2.9%	19%	100%
r_{eff}^f	1.4%	7.5%	1.3%	8.3%	2.3%	12%	50%
v_{eff}^f	8.4%	27%	8.9%	31%	12%	29%	60%
m_r^f	0.005	0.016	0.006	0.018	0.008	0.027	0.14
m_i^f	0.002	0.002	0.003	0.004	0.004	0.006	0.009
ω_A^f	0.010	0.011	0.016	0.019	0.020	0.032	-
Asy^f	0.003	0.005	0.003	0.005	0.004	0.007	-
V_0^c	4.7%	14%	3.2%	10%	3.0%	8.8%	100%
r_{eff}^c	6.7%	16%	3.3%	7.4%	2.0%	6.0%	50%
v_{eff}^c	26%	53%	16%	42%	11%	30%	60%
m_r^c	0.060	0.068	0.052	0.063	0.037	0.056	0.08
m_i^c	0.008	0.009	0.005	0.006	0.003	0.005	0.011
ω_A^c	0.059	0.068	0.044	0.055	0.028	0.044	-
Asy^c	0.024	0.032	0.017	0.024	0.012	0.021	-

[a] $\hat{\epsilon}_P$ and $\hat{\epsilon}_I$ are retrieval error respectively from the P-type and I-type inversions, ϵ_a is the a priori error.

3. Adding the polarization yields better estimates of the aerosol SSA and Asy for both aerosol modes. From P-type inversion, the errors in the retrieved ω_A are lower than 0.02 for aerosols in the fine mode and 0.06 for aerosols in the coarse mode, representing a 10–40% decrease from the I-type inversion. As expected, errors in the Asy also reveal a 30–50% decrease.

6. Conclusion

In this paper, we presented a new algorithm to retrieve both fine- and coarse-mode aerosol properties from multispectral and multiangular solar polarimetric radiation fields such as those measured by AERONET including additional spectra of polarization observations. The retrieval algorithm uses a multicomponent vector radiative transfer model, UNL-VRTM and incorporates the statistical optimized inversion to retrieve aerosol parameters pertaining to a bilognormal particle size distribution (PSD) of spherical aerosols, including the columnar volume concentration, effective radius and variance, and complex indices of refraction. While the new algorithm has heritage from the existing AERONET inversion algorithm in using multiple a priori constraints, it is different from the existing AERONET algorithm in that (a) a bimodal lognormal PSD (instead of 22 size bins) is assumed and (b) the spectral refractive indices are retrievable for both fine and coarse modes.

We applied the new algorithm to a suite of photopolarimetric measurements taken from the new-generation Sun photometer at the Beijing_RADI AERONET station. In order to demonstrate the importance of adding polarization measurements, we performed aerosol retrievals from radiance measurements only (the I-type inversion), in addition to the retrievals using both radiance and polarization measurements (the P-type inversion). We found that, for both types of inversion, the fitting errors for the AOD and sky radiance are much smaller than the calibration uncertainties (0.02 for AOD and 5% for sky radiance). Also, the fitting errors of the degree of linear polarization (DOLP) with the P-type inversion are much smaller than the calibration error (~0.01). However, the DOLP fitting errors in the I-type inversion usually exceed 0.01, and even reach 0.04 for many individual measurements in the case dominated by coarse aerosols, which highlights the necessity to include polarization in the inversion as an additional source of constraint.

Our retrieval results are generally consistent with the AERONET inversion products, but we found distinct differences between the values of the refractive index and SSA for the fine- and coarse-mode aerosols. For these three cases selected for our study, we found that the retrieved real part refractive index is about 1.5–1.6 in the coarse mode, which is higher than those for the fine mode, 1.4–1.5. Also, the coarse-mode aerosols are more absorbing than the fine-mode ones. We also compared the retrieval error for each retrieved parameters between the I-type and P-type inversions. A comparison analysis indicates that the retrieval error can be reduced by at least 50% in PSD parameters, by 10–30% in the refractive index components, and by 10–40% in the aerosol SSA. These error reductions depend on the fine-/coarse-mode

fraction, specifics of instrumentation, and aerosol properties. These improvements in the P-type inversion are consistent with the theoretical analysis in the companion paper of this two-part study [*Xu and Wang*, 2015].

The mode-specific retrieval of aerosol microphysical and optical properties not only facilitates the evaluation of atmospheric chemistry models and the validation of aerosol products from satellite sensors with polarization capability (the challenges we present in section 1) but also can benefit the analysis of aerosol radiative impacts and aerosol chemical compositions. Aerosol radiative forcing depends on both particle size and refractive index [*Nemesure et al*., 1995; *Mishchenko et al*., 2004]. *Nemesure et al*. [1995] have shown that, for sulfate particles, a change of particle size from 0.15 μm to 0.25 μm could lead to an 80% increase of negative forcing. *Mishchenko et al*. [2004] found that accuracies of 10% in r_{eff}, 50% in v_{eff}, and 0.02 in m_{r} are required for radiative forcing calculations that will be able to determine aerosol contributions to the Earth's total energy balance. According to the real retrievals in this paper and the theoretical analysis in the companion paper [*Xu and Wang*, 2015], the accuracies suggested in *Mishchenko et al*. [2004] can only be attained by the integrated use of radiance and polarization. Accurate PSD and real part of refractive index are also needed to identify the aerosol chemical composition, which can be used to derive the aerosol hygroscopicity, to diagnose the efficiency of cloud condensation, and to distinguish anthropogenic aerosol species from natural ones [*Wang et al*., 2008]. Indeed, efforts have been made by using the current AERONET inversions to derive aerosol composition [e.g., *Schuster et al*., 2005; *Arola et al*., 2011; *Li et al*., 2013]. Therefore, with more information on the refractive index, our inversion is expected to provide more robust estimates of the aerosol chemical components.

The promising results in this study are obtained from the initial development and preliminary applications of a new algorithm targeted for the retrieval of aerosol properties from new-generation AERONET measurements. Future developments will include, but not be limited to, the treatment of nonspherical large aerosol particles like mineral dust and the consideration of trimodal aerosols for special situations. While the bilognormal PSD can well represent the aerosol size spectrum in most cases, future research efforts will include the implementation of trimodal aerosol mixtures in situations of cloud formation [*Eck et al*., 2012] or volcanic aerosols [*Eck et al*., 2010]. Moreover, extensive retrievals for a longer period of time will also be performed over sites where CE318-DP Sun photometer instruments have been installed (i.e., Beijing_RADI and Lille). Historically, an issue with the CIMEL polarization measurements has been their limited accuracy [*Li et al*., 2010]. It is thus worthwhile to investigate what level of accuracy in DOLP measurements is necessary to contribute useful information for the retrieval. This question is important not only for the historical polarization measurements by the older CIMEL Sun photometer but also for providing guidance to the new instrument design.

Acknowledgments

This research is supported by a NASA Earth and Space Science Fellowship managed by Mingying Wei, as well as the NASA Radiation Sciences Program and the Glory Mission Program managed by Hal Maring. We acknowledge the data services provided by the AERONET team at NASA GSFC, and the computational support from the Holland Computing Center at the University of Nebraska. The data presented in the manuscript can be available upon request through email to the corresponding author at jwangjun@gmail.com. J. Zeng and J. Wang also thank Qingyuang Han for inspiring them to conduct this work.

References

Arola, A., G. Schuster, G. Myhre, S. Kazadzis, S. Dey, and S. N. Tripathi (2011), Inferring absorbing organic carbon content from AERONET data, *Atmos. Chem. Phys.*, *11*(1), 215–225, doi:10.5194/acp-11-215-2011.

Bodhaine, B. A., N. B. Wood, E. G. Dutton, and J. R. Slusser (1999), On Rayleigh optical depth calculations, *J. Atmos. Oceanic Technol.*, *16*(11), 1854–1861.

Byrd, R. H., P. Lu, J. Nocedal, and C. Zhu (1995), A limited memory algorithm for bound constrained optimization, *SIAM J. Sci. Comput.*, *16*, 1190–1208.

Chin, M., P. Ginoux, S. Kinne, O. Torres, B. N. Holben, B. N. Duncan, R. V. Martin, J. A. Logan, A. Higurashi, and T. Nakajima (2002), Tropospheric aerosol optical thickness from the GOCART model and comparisons with satellite and sun photometer measurements, *J. Atmos. Sci.*, *59*(3), 461–483.

Chowdhary, J., B. Cairns, M. Mishchenko, and L. Travis (2001), Retrieval of aerosol properties over the ocean using multispectral and multiangle photopolarimetric measurements from the Research Scanning Polarimeter, *Geophys. Res. Lett.*, *28*, 243–246, doi:10.1029/2000GL011783.

Chowdhary, J., B. Cairns, and L. D. Travis (2002), Case studies of aerosol retrievals over the ocean from multiangle, multispectral photopolarimetric remote Sensing Data, *J. Atmos. Sci.*, *59*(3), 383–397.

Chowdhary, J., B. Cairns, M. I. Mishchenko, P. V. Hobbs, G. F. Cota, J. Redemann, K. Rutledge, B. N. Holben, and E. Russell (2005), Retrieval of aerosol scattering and absorption properties from photopolarimetric observations over the ocean during the CLAMS experiment, *J. Atmos. Sci.*, *62*(4), 1093–1117.

de Rooij, W. A., and C. C. A. H. van der Stap (1984), Expansion of Mie scattering matrices in generalized spherical functions, *Astron. Astrophys.*, *131*(2), 237–248.

Deuzé, J. L., F. M. Bréon, P. Y. Deschamps, C. Devaux, M. Herman, A. Podaire, and J. L. Roujean (1993), Analysis of the POLDER (POLarization and directionality of Earth's reflectances) airborne instrument observations over land surfaces, *Remote Sens. Environ.*, *45*(2), 137–154.

Deuzé, J. L., et al. (2001), Remote sensing of aerosols over land surfaces from POLDER-ADEOS-1 polarized measurements, *J. Geophys. Res.*, *106*(D5), 4913–4926, doi:10.1029/2000JD900364.

Diner, D. J., et al. (1998), Multi-angle Imaging Spectroradiometer (MISR) instrument description and experiment overview, *Geosci. Remote Sens., IEEE Trans. on*, *36*(4), 1072–1087.

Drury, E., D. J. Jacob, R. J. D. Spurr, J. Wang, Y. Shinozuka, B. E. Anderson, A. D. Clarke, J. Dibb, C. McNaughton, and R. Weber (2010), Synthesis of satellite (MODIS), aircraft (ICARTT), and surface (IMPROVE, EPA-AQS, AERONET) aerosol observations over eastern North America to improve MODIS aerosol retrievals and constrain surface aerosol concentrations and sources, *J. Geophys. Res.*, *115*, D14204, doi:10.1029/2009JD012629.

Dubovik, O. (2004), Optimization of numerical inversion in photopolarimetric remote sensing, in *Photopolarimetry in Remote Sensing*, edited by G. Videen, Y. Yatskiv, and M. Mishchenko, pp. 65–106, Springer, Netherlands.

Dubovik, O., and M. D. King (2000), A flexible inversion algorithm for retrieval of aerosol optical properties from Sun and sky radiance measurements, *J. Geophys. Res.*, *105*(D16), 20,673–20,696, doi:10.1029/2000JD900282.

Dubovik, O., A. Smirnov, B. N. Holben, M. D. King, Y. J. Kaufman, T. F. Eck, and I. Slutsker (2000), Accuracy assessments of aerosol optical properties retrieved from Aerosol Robotic Network (AERONET) Sun and sky radiance measurements, *J. Geophys. Res.*, *105*(D8), 9791–9806, doi:10.1029/2000JD900040.

Dubovik, O., B. Holben, T. F. Eck, A. Smirnov, Y. J. Kaufman, M. D. King, D. Tanre, and I. Slutsker (2002), Variability of absorption and optical properties of key aerosol types observed in worldwide locations, *J. Atmos. Sci.*, *59*(3), 590–608.

Dubovik, O., et al. (2006), Application of spheroid models to account for aerosol particle nonsphericity in remote sensing of desert dust, *J. Geophys. Res.*, *111*, D11208, doi:10.1029/2005JD006619.

Dubovik, O., M. Herman, A. Holdak, T. Lapyonok, D. Tanré, J. L. Deuzé, F. Ducos, A. Sinyuk, and A. Lopatin (2011), Statistically optimized inversion algorithm for enhanced retrieval of aerosol properties from spectral multi-angle polarimetric satellite observations, *Atmos. Meas. Tech.*, *4*(5), 975–1018.

Eck, T. F., et al. (2008), Spatial and temporal variability of column-integrated aerosol optical properties in the southern Arabian Gulf and United Arab Emirates in summer, *J. Geophys. Res.*, *113*, D01204, doi:10.1029/2007JD008944.

Eck, T. F., et al. (2010), Climatological aspects of the optical properties of fine/coarse mode aerosol mixtures, *J. Geophys. Res.*, *115*(D19), D19205, doi:10.1029/2010JD014002.

Eck, T. F., et al. (2012), Fog- and cloud-induced aerosol modification observed by the Aerosol Robotic Network (AERONET), *J. Geophys. Res.*, *117*, D07206, doi:10.1029/2011JD016839.

Halthore, R. N., T. F. Eck, B. L. Markham, and B. N. Holben (1997), Sunphotometric measurements of atmospheric water vapor column abundance in the 940-nm band, *J. Geophys. Res.*, *102*, 4343–4352, doi:10.1029/96JD03247.

Hansen, J. E., and L. D. Travis (1974), Light scattering in planetary atmospheres, *Space Sci. Rev.*, *16*, 572–610.

Hasekamp, O. P., P. Litvinov, and A. Butz (2011), Aerosol properties over the ocean from PARASOL multiangle photopolarimetric measurements, *J. Geophys. Res.*, *116*, D14204, doi:10.1029/2010JD015469.

Holben, B. N., et al. (1998), AERONET—A federated instrument network and data archive for aerosol characterization, *Remote Sens. Environ.*, *66*(1), 1–16.

Holben, B. N., T. F. Eck, I. Slutsker, A. Smirnov, A. Sinyuk, J. Schafer, D. Giles, and O. Dubovik (2006), Aeronet's Version 2.0 quality assurance criteria, *Proc. SPIE Remote Sens. Atmos. Clouds*, *6408*, 64080Q, doi:10.1117/12.706524.

Hovenier, J. W., C. van der Mee, and H. Domke (2004), *Transfer of Polarized Light in Planetary Atmospheres*, 258 pp., Kluwer Acad., Dordrecht, Netherlands.

Kahn, R. A., B. J. Gaitley, M. J. Garay, D. J. Diner, T. F. Eck, A. Smirnov, and B. N. Holben (2010), Multiangle Imaging Spectroradiometer global aerosol product assessment by comparison with the Aerosol Robotic Network, *J. Geophys. Res.*, *115*, D23209, doi:10.1029/2010JD014601.

Kaufman, Y. J., D. Tanré, L. A. Remer, E. F. Vermote, A. Chu, and B. N. Holben (1997), Operational remote sensing of tropospheric aerosol over land from EOS moderate resolution imaging spectroradiometer, *J. Geophys. Res.*, *102*(D14), 17,051–17,067, doi:10.1029/96JD03988.

Levelt, P. F., E. Hilsenrath, G. W. Leppelmeier, G. H. J. van den Oord, P. K. Bhartia, J. Tamminen, J. F. de Haan, and J. P. Veefkind (2006), Science objectives of the ozone monitoring instrument, *Geosci. Remote Sens. IEEE Trans. on*, *44*(5), 1199–1208.

Levy, R. C., L. A. Remer, and O. Dubovik (2007a), Global aerosol optical properties and application to Moderate Resolution Imaging Spectroradiometer aerosol retrieval over land, *J. Geophys. Res.*, *112*, D13210, doi:10.1029/2006JD007815.

Levy, R. C., L. A. Remer, S. Mattoo, E. F. Vermote, and Y. J. Kaufman (2007b), Second-generation operational algorithm: Retrieval of aerosol properties over land from inversion of Moderate Resolution Imaging Spectroradiometer spectral reflectance, *J. Geophys. Res.*, *112*, D13211, doi:10.1029/2006JD007811.

Levy, R. C., L. A. Remer, R. G. Kleidman, S. Mattoo, C. Ichoku, R. Kahn, and T. F. Eck (2010), Global evaluation of the Collection 5 MODIS dark-target aerosol products over land, *Atmos. Chem. Phys.*, *10*(21), 10,399–10,420.

Li, L., Z. Li, K. Li, L. Blarel, and M. Wendisch (2014), A method to calculate Stokes parameters and angle of polarization of skylight from polarized CIMEL Sun/sky radiometers, *J. Quant. Spectros. Radiat. Transfer*, *149*, 334–346.

Li, Z., L. Blarel, T. Podvin, P. Goloub, J.-P. Buis, and J.-P. Morel (2008), Transferring the calibration of direct solar irradiance to diffuse-sky radiance measurements for CIMEL Sun-sky radiometers, *Appl. Opt.*, *47*(10), 1368–1377.

Li, Z., et al. (2009), Improvements for ground-based remote sensing of atmospheric aerosol properties by additional polarimetric measurements, *J. Quant. Spectros. Radiat. Transfer*, *110*(17), 1954–1961.

Li, Z., L. Blarel, T. Podvin, P. Goloub, and L. Chen (2010), Calibration of the degree of linear polarization measurement of polarized radiometer using solar light, *Appl. Opt.*, *49*(8), 1249–1256.

Li, Z., et al. (2013), Aerosol physical and chemical properties retrieved from ground-based remote sensing measurements during heavy haze days in Beijing winter, *Atmos. Chem. Phys.*, *13*(20), 10,171–10,183.

Liou, K. N. (2002), *An Introduction to Atmospheric Radiation*, 583 pp., Academic Press, San Diego, Calif.

Litvinov, P., O. Hasekamp, and B. Cairns (2011), Models for surface reflection of radiance and polarized radiance: Comparison with airborne multi-angle photopolarimetric measurements and implications for modeling top-of-atmosphere measurements, *Remote Sens. Environ.*, *115*(2), 781–792.

Lucht, W., C. B. Schaaf, and A. H. Strahler (2000), An algorithm for the retrieval of albedo from space using semiempirical BRDF models, *Geosci. Remote Sens. IEEE Trans. on*, *38*(2), 977–998.

Maignan, F., F. M. Bréon, and R. Lacaze (2004), Bidirectional reflectance of Earth targets: Evaluation of analytical models using a large set of spaceborne measurements with emphasis on the hot spot, *Remote Sens. Environ.*, *90*(2), 210–220.

Maignan, F., F.-M. Bréon, E. Fédèle, and M. Bouvier (2009), Polarized reflectances of natural surfaces: Spaceborne measurements and analytical modeling, *Remote Sens. Environ.*, *113*(12), 2642–2650.

Martonchik, J. V., R. A. Kahn, and D. J. Diner (2009), Retrieval of aerosol properties over land using MISR observations, in *Satellite Aerosol Remote Sensing Over Land*, edited by A. Kokhanovsky, Springer, Berlin.

Mishchenko, M. I., and L. D. Travis (1997), Satellite retrieval of aerosol properties over the ocean using polarization as well as intensity of reflected sunlight, *J. Geophys. Res.*, *102*(D14), 16,989–17,013, doi:10.1029/96JD02425.

Mishchenko, M. I., and L. D. Travis (1998), Capabilities and limitations of a current FORTRAN implementation of the T-matrix method for randomly oriented, rotationally symmetric scatterers, *J. Quant. Spectros. Radiat. Transfer*, *60*(3), 309–324.
Mishchenko, M. I., L. D. Travis, and D. W. Mackowski (1996), T-matrix computations of light scattering by nonspherical particles: A review, *J. Quant. Spectros. Radiat. Transfer*, *55*(5), 535–575.
Mishchenko, M. I., L. D. Travis, and A. A. Lacis (2002), *Scattering, Absorption, and Emission of Light by Small Particles*, Cambridge Univ. Press, Cambridge.
Mishchenko, M. I., B. Cairns, J. E. Hansen, L. D. Travis, R. Burg, Y. J. Kaufman, J. Vanderlei Martins, and E. P. Shettle (2004), Monitoring of aerosol forcing of climate from space: Analysis of measurement requirements, *J. Quant. Spectros. Radiat. Transfer*, *88*(1–3), 149–161.
Mishchenko, M. I., B. Cairns, J. E. Hansen, L. D. Travis, G. Kopp, C. F. Schueler, B. A. Fafaul, R. J. Hooker, H. B. Maring, and T. Itchkawich (2007), Accurate monitoring of terrestrial aerosols and total solar irradiance: Introducing the glory mission, *Bull. Am. Meteorol. Soc.*, *88*(5), 677–691.
Nadal, F., and F. M. Breon (1999), Parameterization of surface polarized reflectance derived from POLDER spaceborne measurements, *Geosci. Remote Sens. IEEE Trans. on*, *37*(3), 1709–1718.
Nemesure, S., R. Wagener, and S. E. Schwartz (1995), Direct shortwave forcing of climate by the anthropogenic sulfate aerosol: Sensitivity to particle size, composition, and relative humidity, *J. Geophys. Res.*, *100*(D12), 26,105–26,116, doi:10.1029/95JD02897.
Orphal, J., and K. Chance (2003), Ultraviolet and visible absorption cross-sections for HITRAN, *J. Quant. Spectros. Radiat. Transfer*, *82*(1–4), 491–504.
Phillips, D. L. (1962), A technique for the numerical solution of certain integral equations of the first kind, *J. ACM*, *9*(1), 84–97.
Reid, J. S., et al. (2008), An overview of UAE^2 flight operations: Observations of summertime atmospheric thermodynamic and aerosol profiles of the southern Arabian Gulf, *J. Geophys. Res.*, *113*, D14213, doi:10.1029/2007JD009435.
Remer, L. A., et al. (2005), The MODIS aerosol algorithm, products, and validation, *J. Atmos. Sci.*, *62*(4), 947–973.
Rodgers, C. D. (2000), *Inverse Methods for Atmospheric Sounding: Theory and Practice*, World Scientific, Singapore.
Rothman, L. S., et al. (2009), The HITRAN 2008 molecular spectroscopic database, *J. Quant. Spectros. Radiat. Transfer*, *110*(9–10), 533–572.
Schuster, G. L., O. Dubovik, B. N. Holben, and E. E. Clothiaux (2005), Inferring black carbon content and specific absorption from Aerosol Robotic Network (AERONET) aerosol retrievals, *J. Geophys. Res.*, *110*, D10S17, doi:10.1029/2004JD004548.
Schuster, G. L., O. Dubovik, and B. N. Holben (2006), Angstrom exponent and bimodal aerosol size distributions, *J. Geophys. Res.*, *111*, D07207, doi:10.1029/2005JD006328.
Seinfeld, J. H., and S. N. Pandis (2006), *Atmospheric Chemistry and Physics: From Air Pollution to Climate Change*, 2nd ed., 1232 pp., John Wiley Inc., Hoboken, N. J.
Smirnov, A., B. N. Holben, T. F. Eck, O. Dubovik, and I. Slutsker (2000), Cloud-screening and quality control algorithms for the AERONET database, *Remote Sens. Environ.*, *73*(3), 337–349.
Spurr, R. (2006), VLIDORT: A linearized pseudo-spherical vector discrete ordinate radiative transfer code for forward model and retrieval studies in multilayer multiple scattering media, *J. Quant. Spectrosc. Radiat. Transfer*, *102*, 316–342.
Spurr, R. J. D. (2004), A new approach to the retrieval of surface properties from earthshine measurements, *J. Quant. Spectros. Radiat. Transfer*, *83*(1), 15–46.
Spurr, R., J. Wang, J. Zeng, and M. I. Mishchenko (2012), Linearized T-matrix and Mie scattering computations, *J. Quant. Spectros. Radiat. Transfer*, *113*(6), 425–439.
Twomey, S. (1963), On the numerical solution of fredholm integral equations of the first kind by the inversion of the linear system produced by Quadrature, *J. ACM*, *10*(1), 97–101.
Twomey, S. (1977), *Introduction to the Mathematics of Inversion in Remote Sensing and Indirect Measurements*, 243 pp., Dover Publ., Inc., Mineola, New York.
Wang, J., and S. T. Martin (2007), Satellite characterization of urban aerosols: Importance of including hygroscopicity and mixing state in the retrieval algorithms, *J. Geophys. Res.*, *112*, D17203. doi:10.1029/2006JD008078.
Wang, J., X. Liu, S. A. Christopher, J. S. Reid, E. Reid, and H. Maring (2003), The effects of non-sphericity on geostationary satellite retrievals of dust aerosols, *Geophys. Res. Lett.*, *30*(24), 2293. doi:10.1029/2003GL018697.
Wang, J., D. J. Jacob, and S. T. Martin (2008), Sensitivity of sulfate direct climate forcing to the hysteresis of particle phase transitions, *J. Geophys. Res.*, *113*, D11207, doi:10.1029/2007JD009368.
Wang, J., X. Xu, R. Spurr, Y. Wang, and E. Drury (2010), Improved algorithm for MODIS satellite retrievals of aerosol optical thickness over land in dusty atmosphere: Implications for air quality monitoring in China, *Remote Sens. Environ.*, *114*(11), 2575–2583.
Wang, J., X. Xu, D. K. Henze, J. Zeng, Q. Ji, S.-C. Tsay, and J. Huang (2012), Top-down estimate of dust emissions through integration of MODIS and MISR aerosol retrievals with the GEOS-Chem adjoint model, *Geophys. Res. Lett.*, *39*, L08802, doi:10.1029/2012GL051136.
Wang, J., X. Xu, S. Ding, J. Zeng, R. Spurr, X. Liu, K. Chance, and M. Mishchenko (2014), A numerical testbed for remote sensing of aerosols, and its demonstration for evaluating retrieval synergy from a geostationary satellite constellation of GEO-CAPE and GOES-R, *J. Quant. Spectros. Radiat. Transfer*, *146*, 510–528.
Wanner, W., X. Li, and A. H. Strahler (1995), On the derivation of kernels for kernel-driven models of bidirectional reflectance, *J. Geophys. Res.*, *100*(D10), 21,077–21,089, doi:10.1029/95JD02371.
Waquet, F., P. Goloub, J. L. Deuzé, J. F. Léon, F. Auriol, C. Verwaerde, J. Y. Balois, and P. François (2007), Aerosol retrieval over land using a multiband polarimeter and comparison with path radiance method, *J. Geophys. Res.*, *112*, D11214, doi:10.1029/2006JD008029.
Waquet, F., B. Cairns, K. Knobelspiesse, J. Chowdhary, L. D. Travis, B. Schmid, and M. I. Mishchenko (2009), Polarimetric remote sensing of aerosols over land, *J. Geophys. Res.*, *114*, D01206, doi:10.1029/2008JD010619.
Xiao, Y., and H. Zhang (2008), Modified subspace limited memory BFGS algorithm for large-scale bound constrained optimization, *J. Comput. Appl. Math.*, *222*(2), 429–439.
Xu, X., and J. Wang (2015), Retrieval of aerosol microphysical properties from AERONET photo-polarimetric measurements: 1. Information content analysis, *J. Geophys. Res. Atmos.*, *120*, doi:10.1002/2015JD023108.
Xu, X., J. Wang, D. K. Henze, W. Qu, and M. Kopacz (2013), Constraints on aerosol sources using GEOS-Chem adjoint and MODIS radiances, and evaluation with multisensor (OMI, MISR) data, *J. Geophys. Res. Atmos.*, *118*, 6396–6413, doi:10.1002/jgrd.50515.
Yang, Z., J. Wang, C. Ichoku, E. Hyer, and J. Zeng (2013), Mesoscale modeling and satellite observation of transport and mixing of smoke and dust particles over northern sub-Saharan African region, *J. Geophys. Res. Atmos.*, *118*, 12,139–12,157, doi:10.1002/2013JD020644.
Zhu, C., R. H. Byrd, P. Lu, and J. Nocedal (1994), L-BFGS-B: A limited memory FORTRAN code for solving bound constrained optimization problems, *Technique Report Rep.*, Northwestern Univ.